THE SEA: THE SCIENCE OF OCEAN PREDICTION
Journal of Marine Research, 75, 765–813, 2017

A future for intelligent autonomous ocean observing systems

by P.F.J. Lermusiaux[1,2], D.N. Subramani[1], J. Lin[1], C.S. Kulkarni[1], A. Gupta[1], A. Dutt[1], T. Lolla[1], P.J. Haley Jr.[1], W.H. Ali[1], C. Mirabito[1], and S. Jana[1]

ABSTRACT

Ocean scientists have dreamed of and recently started to realize an ocean observing revolution with autonomous observing platforms and sensors. Critical questions to be answered by such autonomous systems are where, when, and what to sample for optimal information, and how to optimally reach the sampling locations. Definitions, concepts, and progress towards answering these questions using quantitative predictions and fundamental principles are presented. Results in reachability and path planning, adaptive sampling, machine learning, and teaming machines with scientists are overviewed. The integrated use of differential equations and theory from varied disciplines is emphasized. The results provide an inference engine and knowledge base for expert autonomous observing systems. They are showcased using a set of recent at-sea campaigns and realistic simulations. Real-time experiments with identical autonomous underwater vehicles (AUVs) in the Buzzards Bay and Vineyard Sound region first show that our predicted time-optimal paths were faster than shortest distance paths. Deterministic and probabilistic reachability and path forecasts issued and validated for gliders and floats in the northern Arabian Sea are then presented. Novel Bayesian adaptive sampling for hypothesis testing and optimal learning are finally shown to forecast the observations most informative to estimate the accuracy of model formulations, the values of ecosystem parameters and dynamic fields, and the presence of Lagrangian Coherent Structures.

Keywords: adaptive sampling, path planning, reachability, Gaussian mixture models, dynamically orthogonal equations, GMM-DO filter, mutual information, hierarchical Bayesian model learning, machine learning, science of autonomy, ALPS, expert systems

1. Introduction

Observing the ocean has been and continues to be critical to humans. The marine environment, with its ever changing forms, fascinates minds. The understanding of its inner-workings has motivated scientists for a long time. Since the early days, other than for fixed platforms, the norm for ocean science observations has been expeditionary, with research

1. Department of Mechanical Engineering, Massachusetts Institute of Technology, Room 5-207B, 77 Massachusetts Avenue, Cambridge, MA 02139-43071
2. Corresponding author: ***e-mail: pierrel@mit.edu***

vessels collecting multidisciplinary measurements (e.g., Dickey 2003; Schofield et al. 2010). In the past decades, with the advent of computing devices and automation, such adventurous and often risky expeditions have been augmented with, or replaced by, varied robotics-based platforms and sensors (e.g., Rudnick and Perry 2003; Bellingham and Rajan 2007; Nicholson and Healey 2008). A first class of sensing platforms are autonomous underwater vehicles (AUVs) with a speed relative to the ocean currents (Curtin et al. 1993; Griffiths et al. 2001). Such platforms include propelled AUVs (Bellingham et al. 1992; Schmidt et al. 1996; Manley 2004; Freitag et al. 2005) and underwater gliders (Eriksen et al. 2001; Sherman et al. 2001; Webb, Simonetti, and Jones 2001; Schofield et al. 2007; Meyer 2016). Also among such vehicles with relative speeds are the solar-powered vehicles (Crimmins et al. 2006; Carragher et al. 2013), wave gliders (Manley and Willcox 2010; Daniel et al. 2011), and other varied surface crafts (Curcio et al. 2005; Xu et al. 2008; Brizzolara and Brizzolara 2016; Liu et al. 2016). Considering the more Lagrangian observations, the large number of autonomous drifters (Davis 1991; Niiler 2001; Lumpkin and Pazos 2007; Centurioni et al. 2017a) and of floats (Swallow 1955; Swallow, McCartney, and Millard 1974; Roemmich et al. 2001; Davis, Sherman, and Dufour 2001; Roemmich et al. 2004, 2009; Riser et al. 2016) that presently roam the world's oceans provide large data sets. Related platforms are the hybrid profilers (Pinkel et al. 2011; Lucas et al. 2016), the miniature autonomous underwater explorers (Jaffe et al. 2017), and other semi-drifting surface crafts. Many of these new robotic capabilities have led to multidisciplinary ocean science results and discoveries, from larger scales to (sub)mesoscales (e.g., Abbott et al. 1990; Rudnick et al. 2004; Davis et al. 2008; Martin et al. 2009; Ramp et al. 2009; Gawarkiewicz et al. 2011; Mahadevan et al. 2012; Todd et al. 2012; Rudnick 2016 and references therein), and from submesoscales to turbulence (e.g., St Laurent and Thurnherr 2007; Boyd et al. 2010; Lavender, Davis, and Owens 2002; Rainville et al. 2013; Johnston and Rudnick 2015; Farrar et al. 2015; Shcherbina et al. 2015). Recent technological advances include better designs and reliability, reduced biofouling, more efficient power systems, and faster computers (e.g., Yuh 2000; Bachmayer et al. 2004; Fiorelli et al. 2006; Bellingham and Rajan 2007; Bahr, Leonard, and Fallon 2009). They also consist of more accurate theory and powerful methods and algorithms (e.g., Latombe 1991; LaValle 2006; Curtin and Bellingham 2009; Leonard et al. 2007, 2010; Ferrari et al. 2016; Lermusiaux et al. 2016; Wolek and Woolsey 2017). With all such technologies, a wealth of autonomous ocean observing possibilities are knocking at the door.

Visionary ocean scientists have dreamed (Stommel 1989) and, as reviewed above, started this autonomous ocean observing revolution with robotics. Such platforms reduce the traditional undersampling of ocean surveys and augment satellite data. A critical property of most robotic platforms is that they are significantly affected by the dynamic ocean motions, including currents and waves. This is true not only for drifting devices but also for gliders, which are often slower than common currents, and for propelled AUVs that often have nominal speeds comparable with that of strong currents (Schmidt et al. 1996; Elisseeff et al. 1999; Yan et al. 2014). Their ocean measurements are thus a mixture of Eulerian

(fixed or not affected by currents) and Lagrangian (current-following) observations. These facts are crystallized in the name "Autonomous and Lagrangian Platforms and Sensors" (ALPS) (e.g., Rudnick and Perry 2003; Dickey et al. 2008 and references therein). To account for environmental effects on the vehicles, researchers teamed up to use predictive models and control algorithms to help with platform piloting and sensing. In addition to previously cited efforts, a major collaborative endeavor is the Autonomous Ocean Sampling Network (AOSN) and subsequent related projects (e.g., Curtin et al. 1993; Glenn et al. 2000; Rudnick et al. 2004; Leonard et al. 2007, 2010; Paley, Zhang, and Leonard 2008; Davis, Leonard, and Fratantoni 2009; Ramp et al. 2009; Haley et al. 2009; Curtin and Bellingham 2009).

Some ocean observers may still wonder why dynamic models or fancy controls should be used by autonomous observing systems. One could, however, conversely argue that even in pure explorations, one always has a predictive model and some control law, even if implicit or unknown to the explorer. For example, a ship survey is often planned based on the ship capabilities and on prior models such as the expected scales of the processes to be measured, conservation laws, statistical models, or some other predictions. Even if only implicit, there is thus some sort of prior predictive model and control law.

In marine robotics, predictive ocean models provide information about the evolution of the environment and vehicle models describe the dynamic motions of the robotic platforms. In such models, regardless of their simplicity or complexity, not only the model equations are inexact, or at least uncertain, but also the inputs to these equations (Lermusiaux et al. 2006; Dhanak and Xiros 2016; Penland and Navarra 2017). All prior models and control laws are thus approximate especially for multiscale dynamics and multiresolution observation systems. Uncertainties should thus be accounted for in guiding ocean vehicles, both for the dynamics to be observed and for the path planning of the vehicle.

Many forecasting ocean models are complex computational systems that employ advanced numerical schemes (Haidvogel et al. 2017) to solve fundamental differential equations governing the conservation of mass, momentum, energy, and salt in the ocean (Jacobs and Fox-Kemper 2017; Treguier et al. 2017) under the influence of several forcing and interactions such as tides (Egbert and Ray 2017), atmospheric fluxes (Miller et al. 2017; Pullen et al. 2017), surface waves (Babanin et al. 2017), and sea ice (Bertino and Holland 2017). To increase accuracy of model predictions, ocean observations are combined with models through data assimilation (Robinson, Lermusiaux, and Sloan III 1998; Robinson and Lermusiaux 2002; Kalnay 2003; Särkkä 2013). Because the ocean remains undersampled, determining where, when, and what to sample for optimal information, and how to optimally reach the sampling locations, are critical questions to be answered. Answering them using quantitative predictions and fundamental principles for optimal observations calls for the reproducible, methodical integration of ocean dynamics, ocean modeling, data assimilation, control theory, information theory, machine learning, and automation. Such integration is not yet common, in part because of the many challenges of interdisciplinary research. The future for autonomous observing systems should, however, strongly

benefit from such methodical integration and the related emerging marine science of autonomy (Steinberg 2006). The present manuscript reviews progress and directions toward this future.

In what follows, we first define and outline concepts relevant to the marine science of autonomy and overview fundamental reproducible results obtained in reachability and path planning, adaptive sampling, machine learning, and teaming machines with scientists (Section 2). We then present a set of recent at-sea campaigns and realistic simulations that showcase capabilities and benefits of using such quantitative methods and fundamental equations to provide the inference engine and knowledge base of expert observing systems (Section 3). Conclusions are provided in Section 4.

2. Marine science of autonomy

The science of autonomy can be defined as the "systematic development of fundamental knowledge about autonomous decision making and task completing in the form of testable autonomous methods, models, and systems" (Lermusiaux et al. 2016). In this section, we review concepts and results relevant to the marine science of autonomy for observing systems. The focus is on methods and models for reachability, path planning, and adaptive sampling, and on the use of machine learning and the addition of scientific knowledge and inference engines to form expert observing systems (Jackson 1998; Russell and Norvig 2009). We note that the review does not cover several critical components of robotic systems such as nested autonomy (e.g. Benjamin et al. 2010; Schmidt et al. 2016), underwater navigation, communication, and motion control (e.g. Mahmoudian and Woolsey 2008; Leonard and Bahr 2016), or ocean sensing and underwater networks (e.g. Heidemann, Stojanovic, and Zorzi 2011; Venkatesan et al. 2018).

a. Reachability and path panning

The ability to predict and control the behavior of ALPS in dynamic currents is essential for efficient observing systems. Such quantitative planning enables accurate predictions of reachable regions, optimal launch and recovery, and optimal paths for ocean vehicles (Fig. 1). Some key questions are as follows: (i) What are the locations that can be visited by an autonomous platform released at some position and time? (ii) Are there ideal locations and strategies for optimal pick-up and interception? (iii) How to compute exact time-optimal, energy-optimal, and/or safe paths for navigating vehicles? (iv) Are the equations and methods to answer the above questions scalable and practical for real-time expert observing systems? In what follows, we first define concepts and overview prior results. We then present differential equations and theory that address these questions.

i. Concepts and prior results. The prediction of paths along which specific criteria (e.g., time, energy, data collected, and/or safety) are optimized is called path planning. Traditionally, path planning has been developed for robots in static environments (e.g., LaValle

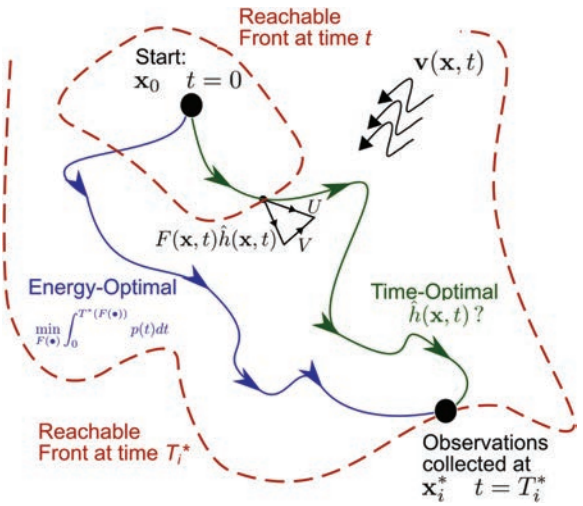

Figure 1. Schematic of reachability and path planning. Reachable sets, fronts, and optimal paths are sketched for a vehicle operating at nominal speed $F(\mathbf{x}, t)$ within dynamic currents $\mathbf{v}(\mathbf{x}, t)$. The total vehicle velocity U is the vector sum of the nominal velocity and currents at that location and time. The optimal arrival time T_i^* at each optimal sampling position $\mathbf{x}_i^*$ is the first time at which the reachability front crosses $\mathbf{x}_i^*$. For nominal vehicle speeds independent of the local heading, the time-optimal path (green) is such that the vehicle headings are normal to the reachability front at every time. For energy-optimal paths (blue) we compute the nominal speed function $F(\bullet)$ that minimize the energy consumption through an efficient stochastic optimization procedure. Predictions can be done in 2D or 3D, and for deterministic or stochastic currents $\mathbf{v}(\mathbf{x}, t; \omega)$. For stochastic currents, we employ ensembles or efficient dynamically orthogonal equations to evaluate distributions of reachable sets, fronts, and optimal paths.

2006); however, in the ocean, dynamic currents significantly affect the motion of vehicles. Traditional planning algorithms then often provide incorrect solutions or are too expensive for real-time use.

In recent years, several approaches have been proposed to extend planning methods for static environments to marine vehicles. Many are based on graphs and dynamic programming such as Dijkstra's method and the A* algorithm (Carroll et al. 1992; Garau et al. 2009; Rao and Williams 2009; Frolov, Garau, and Bellingham 2014). The key issue in the A* algorithm is the choice of a heuristic that is often difficult to define. Thus, optimality is not guaranteed in complex ocean flows, and results are useful mostly in simple steady flows (Rao and Williams 2009; Lolla et al. 2012). Recently, a time-dependent Dijkstra's algorithm has been utilized for time-optimal routing of ships considering the effect of surface waves (Mannarini et al. 2016) and extended for currents (Mannarini et al. 2017). Fast marching methods (Sethian 1999) for flow-dependent cost functions were used by Petres et al. (2007). The Eikonal equation that is solved provides time-optimality, but only when the vehicle speed is always larger than ocean currents. Soulignac, Taillibert, and Rueher

(2009) and Thompson et al. (2009, 2010) developed a related idea of wave front expansions for planning underwater vehicle paths. Some authors have focused on obstacle avoidance with potential field methods (Witt and Dunbabin 2008) and Voronoi diagrams (Bakolas and Tsiotras 2010).

Other planners employ optimization methods such as nonlinear programming (Inanc, Shadden, and Marsden 2005; Zhang et al. 2008), direct (Kruger et al. 2007) or iterative nonlinear optimization (Jones and Hollinger 2017), and evolutionary algorithms (Alvarez, Caiti, and Onken 2004; Aghababa 2012) to generate time- and energy optimal paths that minimize a cost function. Here, the computational cost grows exponentially for classic deterministic optimization and a solution is not guaranteed in evolutionary algorithms. Yet other classes use case-based reasoning (Vasudevan and Ganesan 1994) or dynamics-based methods such as detecting and following Lagrangian coherent structures to minimize energy consumption (Hsieh et al. 2012; Michini et al. 2014). Uncertainties in the ocean are usually incorporated by Monte Carlo methods where the deterministic plan is computed for each ensemble member, hence, leading to the statistics of optimal paths (e.g. Wang et al. 2016). Markov decision process with several variations have also been employed to account for ocean uncertainty (Hollinger et al. 2016).

ii. Reachability and path panning with differential equations: Reachability and time-optimality. As schematized on Figure 1, we studied the problem of path planning through the fundamental concept of reachability (Bryson 1975) and employed exact partial differential equations (PDEs) that govern reachability fronts (Lolla et al. 2012, 2014a,b). The set of locations that can be reached is the reachable set and its boundary is called the reachability front. The net motion of autonomous vehicles is the sum of the forward thrust (due to propulsion or buoyancy changes, for example) and advection by dynamic currents. Based on these first principles, Lolla et al. (2014a) developed rigorous theories and a PDE (a modified Hamilton–Jacobi level-set equation) whose solution tracks the evolution of the reachability front of a vehicle moving in strong and dynamic flows.

Consider the motion of a vehicle from the start point ($\mathbf{x}_0$) to the destination ($\mathbf{x}_i^*$) in the domain $\Omega \subseteq \mathbb{R}^n$ that experiences an uncertain dynamic velocity field $\mathbf{V}(\mathbf{x}, t; \omega) : \Omega \times [0, \infty) \to \mathbb{R}^n$, where ω represents the specific realization of the flow field, here the uncertain ocean currents. The *maximum* speed of the vehicle relative to the currents is denoted by $F(\mathbf{x}, t, \hat{\mathbf{h}}; \mu)$. This nominal speed is in general a function of the spatial location ($\mathbf{x}$), present time (t), and heading direction $\hat{\mathbf{h}}$. The parameter μ represents a specific realization of the vehicle speed that allows for its optimization according to an objective function. Both the external velocity field $\mathbf{V}(\mathbf{x}, t; \omega)$ and the nominal speed $F(\mathbf{x}, t, \hat{\mathbf{h}}; \mu)$ are assumed to be Lipschitz continuous and bounded in all their respective arguments.

The growth of the reachable set is governed by a modified Hamilton–Jacobi level-set equation (Lolla et al. 2014a,b). The reachability front (boundary of the reachable set) is embedded as the zero level set of a signed distance function (ϕ; also called the level-set function) initialized with respect to the start position of the vehicle (see Fig. 1). Note that as

we account for uncertainty in the external velocity field (denoted by the realization or event ω) and for the many possible nominal vehicle speed function (denoted by the realization μ), the level-set function will be stochastic, dependent on both ω and μ. The growth of ϕ is governed by a stochastic PDE (S-PDE), given by equation (1), to be understood in the viscosity solution sense (Crandall and Lions 1983),

$$\frac{\partial \phi(\mathbf{x}, t; \omega, \mu)}{\partial t} + \max_{\hat{\mathbf{h}}} \left(F(\mathbf{x}, t, \hat{\mathbf{h}}; \mu) \cdot \nabla \phi(\mathbf{x}, t; \omega, \mu) \right) + \mathbf{V}(\mathbf{x}, t; \omega) \cdot \nabla \phi(\mathbf{x}, t; \omega, \mu) = 0 \,. \tag{1}$$

In (1), we refer to the second term as the "optimal propulsion term," as it optimizes the effect of the vehicle motion on the evolution of the level-set function. The optimal vehicle headings ($\hat{\mathbf{h}}^*(\mathbf{x}, t; \omega, \mu)$) are computed by maximizing the propulsion term, $F(\mathbf{x}, t, \hat{\mathbf{h}}; \mu) \cdot \nabla \phi(\mathbf{x}, t; \omega, \mu)$, over all the possible heading directions ($\hat{\mathbf{h}}$). The third term is referred to as the "advection term," as it is the evolution due to the external velocity field.

When the speed of vehicles does not depend on their heading direction, the maximum nominal speed becomes $F(\mathbf{x}, t; \mu)$. The optimal vehicle heading ($\hat{\mathbf{h}}^*$) is then always in the normal direction to the local level set (Lolla et al. 2014a) and equation (1) simplifies to

$$\frac{\partial \phi(\mathbf{x}, t; \omega, \mu)}{\partial t} + F(\mathbf{x}, t; \mu) |\nabla \phi(\mathbf{x}, t; \omega, \mu)| + \mathbf{V}(\mathbf{x}, t; \omega) \cdot \nabla \phi(\mathbf{x}, t; \omega, \mu) = 0 \,. \tag{2}$$

iii. Reachability and path panning with differential equations: Time-optimal paths. The first time at which the reachability front of the vehicle reaches the target point is the optimal travel time (T_i^*). Further, the optimal path is a characteristic of equations (1) or (2) that passes through the target (Lolla et al. 2014a). When fields are sufficiently regular, this trajectory (denoted by $\mathbf{Y}(t; \omega, \mu)$) is computed by solving the ordinary differential equation (3) backwards in time, starting from the target, as the optimal heading direction ($\hat{\mathbf{h}}^*$) is simply the normal to the local reachability front,

$$\frac{d\mathbf{Y}(t; \omega, \mu)}{dt} + \mathbf{V}(\mathbf{Y}, t; \omega) + F(\mathbf{Y}, t, \hat{\mathbf{h}}^*(t); \mu) \cdot \hat{\mathbf{h}}^*(t) = 0 \,. \tag{3}$$

The actual path used by the marine vehicle is selected from the set of realizations of optimal trajectories governed by this equation (3). For the cases where the ocean flow is uncertain (ω), the actual optimal path selected from among all these optimal realizations can be the path realization that minimize risks for a given risk profile of the user (Subramani, Wei, and Lermusiaux 2018) or some other uncertainty/time metrics (Lermusiaux et al. 2016). For the cases where the uncertainty is artificial (μ), the actual optimal path is selected by optimization of an objective function, e.g., total energy expenditure for a given arrival time, as will be discussed below.

iv. Reachability and path panning with differential equations: Deterministic time-optimal path planning. To plan shortest-time paths in deterministic flow fields, for vehicles whose

speeds depend on their heading direction, equation (1) is reduced to the partial differential equation (4) by eliminating all uncertainty in the external flow field,

$$\frac{\partial \phi(\mathbf{x}, t)}{\partial t} + \max_{\hat{\mathbf{h}}} \left(F(\mathbf{x}, t, \hat{\mathbf{h}}) \cdot \nabla \phi(\mathbf{x}, t) \right) + \mathbf{V}(\mathbf{x}, t) \cdot \nabla \phi(\mathbf{x}, t) = 0 \, . \tag{4}$$

When the maximum nominal vehicle speed is also independent of the local heading, the growth of the deterministic reachability front, i.e., equations (2) or (4), simplifies to equation (5),

$$\frac{\partial \phi(\mathbf{x}, t)}{\partial t} + F(\mathbf{x}, t) |\nabla \phi(\mathbf{x}, t)| + \mathbf{V}(\mathbf{x}, t) \cdot \nabla \phi(\mathbf{x}, t) = 0 \, , \tag{5}$$

where the maximum possible nominal vehicle speed is utilized at all times (denoted by the single realization $F(\mathbf{x}, t)$). The optimal paths are governed by the deterministic reduction of the general equation (3).

We extended these equations to plan time-optimal paths while maintaining specific formations for swarms of autonomous vehicles, as well as avoiding static and dynamic obstacles (Lolla et al. 2015). We applied our equations for reachability analysis in the Sulu Sea (Lolla et al. 2014b) and for coordinated path planning of glider swarms in complex archipelagos (Lolla et al. 2015; Fig. 2f). Further, accurate and consistent numerical schemes were developed to solve a novel nondimensional form of the above mentioned equations in three dimensions and incorporating the operational constraints of real marine vehicles, such as gliders and floats, as well as surface vehicles such as sail-boats and kayaks (Kulkarni 2017; Lolla and Lermusiaux 2018; Fig. 2a). Fundamental governing equations for reachability and safe and optimal routing of ships were also developed and implemented (Fig. 2g). Recent applications of our theory and software at work in real time with REMUS 600 AUVs in coastal regions are showcased in Section 3a.

v. Reachability and path panning with differential equations: Stochastic time-optimal path planning. To account for uncertainties in the ocean flow, we keep the uncertainty (denoted by the realization ω) in the external velocity field $\mathbf{V}$. Simplifying equation (2), the result is then the S-PDE, equation (6), that governs the evolution of the stochastic reachability fronts in uncertain flows (Wei 2015; Subramani, Wei, and Lermusiaux 2018),

$$\frac{\partial \phi(\mathbf{x}, t; \omega)}{\partial t} + F(\mathbf{x}, t) |\nabla \phi(\mathbf{x}, t; \omega)| + \mathbf{V}(\mathbf{x}, t; \omega) \cdot \nabla \phi(\mathbf{x}, t; \omega) = 0 \, . \tag{6}$$

We note that if we start from equation (1) instead of equation (2), we extend equation (6) to the case of maximum nominal vehicle speeds dependent of the local heading (not given here for brevity). To solve these S-PDEs equation (6), we employed ensembles of ocean forecasts, for example during recent sea experiments with floats in the Northern Arabian Sea (cf., Section 3b). We also utilized our efficient dynamically orthogonal stochastic level-set equations for accurate and fast (2–4 orders of magnitude compared with ensemble methods) stochastic planning (Subramani, Wei, and Lermusiaux 2018), both for analytical examples (Fig. 2d) and realistic simulations.

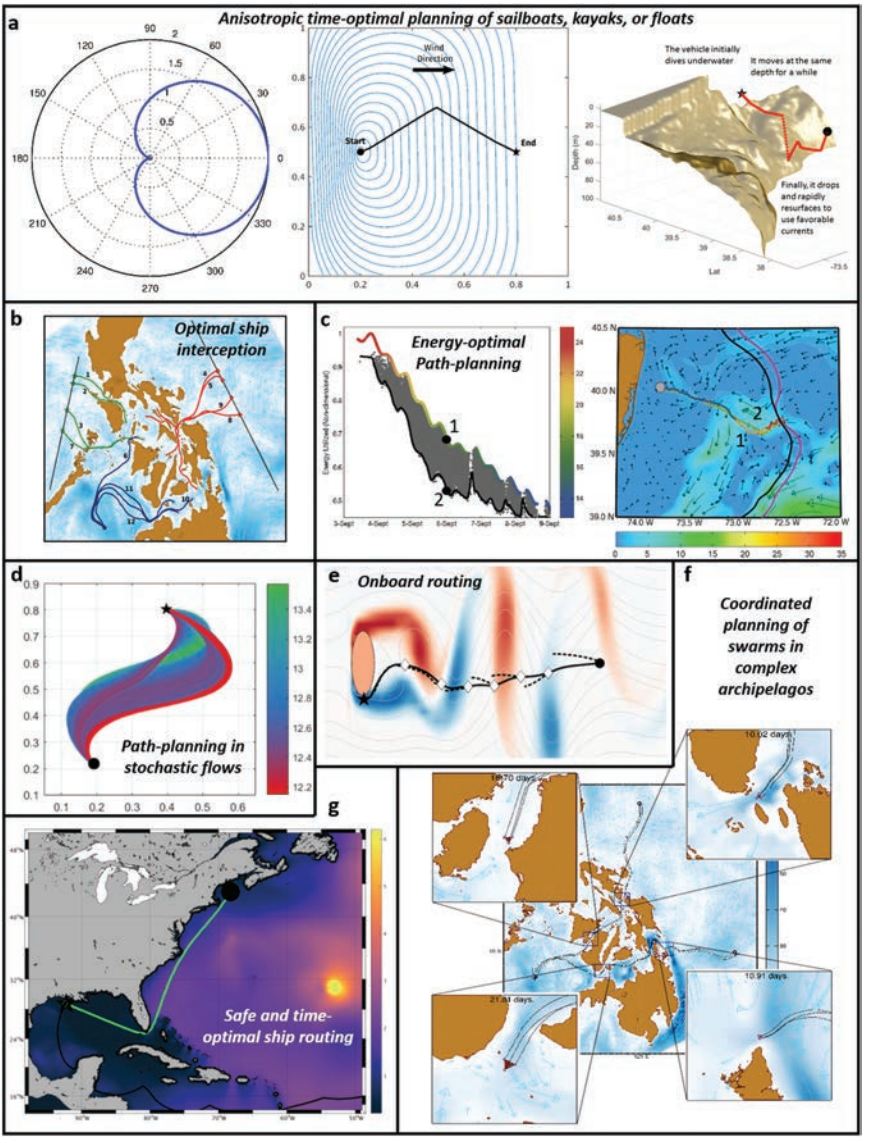

Figure 2. Varied applications of Massachusetts Institute of Technology Multidisciplinary Simulation Estimation and Assimilation System (MIT MSEAS) optimal path planning. **(a)** Modified level-set equations predict optimal trajectories for sailboats and floats, whose speeds vary with the direction of travel. Shown are the velocity-heading dependency and time-optimal path for a sailboat traveling downwind (Lolla and Lermusiaux 2018), and the 3-dimensional time-optimal trajectory for a marine float (Kulkarni 2017). **(b)** Optimal trajectories of twelve gliders for a fastest-time picked up by either two underway ships or a fixed station (e.g., mooring) (Lolla 2016). **(c)** Energy-optimal glider #2 consumes 26% less energy than constant-speed glider #1. The distribution of vehicle speed, energy

Figure 2. (continued) usage, and arrival times are computed by efficient dynamically orthogonal (DO) level-set equations (Subramani, Haley, and Lermusiaux 2017). **(d)** Stochastic time-optimal paths in a stochastic double-gyre flow colored with their respective optimal arrival times (Subramani, Wei, and Lermusiaux 2018). **(e)** As new data become available, ocean forecasts, and thus also optimal paths, are updated by data assimilation, leading to adaptive or onboard routing. **(f)** Dynamic coordination of two glider groups that maintain an equilateral triangle formation in the Philippines region. Final trajectories (38 days after the deployment) are superimposed on the vertically-averaged flow field of horizontal currents on the 38th day. Flow patterns (curved vectors) are overlaid by colored flow magnitude. Magnified views of the region enclosed by the dotted squares are shown at corresponding times (Lolla, Haley, and Lermusiaux 2015). **(g)** Safe and optimal route (green line) of a tanker traveling from Boston to Houston during a severe storm, overlaid on a color plot of significant wave height (in m) at the starting time.

vi. Reachability and path panning with differential equations: Energy-optimal path planning. Saving energy to increase the duration of sampling missions is useful for ocean research. The energy consumption of ocean vehicles can be modeled in terms of vehicle speed and acceleration. For energy-optimal planning, the question is what speed time-series (engine thrust) and headings should be followed by the vehicle to minimize energy usage for a given travel time (Fig. 1) between sampling locations. This is accounted for by using an artificial uncertainty (denoted by the realization μ) in the vehicle speed function to be optimized (F). Simplifying equation (2), the result is the S-PDE (7) (e.g., Subramani and Lermusiaux 2016; Subramani, Haley, and Lermusiaux 2017).

$$\frac{\partial \phi(\mathbf{x}, t; \mu)}{\partial t} + F(\mathbf{x}, t; \mu)|\nabla \phi(\mathbf{x}, t; \mu)| + \mathbf{V}(\mathbf{x}, t) \cdot \nabla \phi(\mathbf{x}, t; \mu) = 0 \tag{7}$$

Such energy-optimal speed time-series, headings, and paths are computed by a rigorous stochastic optimization using the dynamically orthogonal field equations (Subramani and Lermusiaux 2016) over the distribution of vehicle speed time series and corresponding time-optimal arrival times and energy consumption. This energy optimal path planning was employed for gliders in realistic coastal ocean re-analyses for the Middle Atlantic Bight and Shelfbreak front region (Subramani, Haley, and Lermusiaux 2017; Fig. 2c), resulting in up to 26% energy savings when compared with constant-speed time-optimal paths.

vii. Reachability and path panning with differential equations: Optimal pick-up and interception. To save time and costs in ocean sampling, the launch, pick-up, and/or interception of autonomous platforms should be efficient. Pursuit-evasion differential games are those in which a group of pursuers attempt to intercept a group of active evaders. In Sun et al. (2017a, b), reachability analysis is applied to discover optimal strategies for pursuers in canonical dynamic flow fields. These ideas are directly applicable for recovery and optimal pick-up of vehicles in real-time sampling operations (Fig. 2b). They can also be directly used for ship interceptions (Mirabito et al. 2017).

viii. Reachability and path panning with differential equations: Realistic planning and computational costs. The reachable sets, fronts, and optimal paths can be predicted, depending on applications, in 2D or 3D space (Kulkarni 2017), for isotropic and anisotropic motions (Lolla and Lermusiaux 2018), and for several types of ocean vehicles such as floats, gliders (Lolla et al. 2014a,b; Subramani, Haley, and Lermusiaux 2017), propelled vehicles (Subramani et al. 2017), and surface kayaks or ships in wave conditions (Mirabito et al. 2017).

Today, the computational time for all of these applications is much shorter than the mission time, even with a single CPU. For example, for reachability and time-optimal planning, the computational time is of the order of seconds to minutes for days to weeks of sampling missions. Importantly, the cost only grows linearly with the spatial and temporal resolution. Even for large stochastic energy-optimal planning, the computational time scales linearly with the size of the stochastic subspace (which is O(100)) and this time is less than (or of the order of) the time required to integrate modern numerical ocean modeling systems. All of such planning can thus be re computed multiple times in real-time and as new observations arrive, hence allowing feedback and onboard routing (Fig. 2e). In Section 3b, we show examples of our real-time reachability predictions and probability maps for the Northern Arabian Sea Circulation-Autonomous Research (NASCar) program.

b. Adaptive sampling

Different types of sensors have been utilized with autonomous platforms to collect information of all kinds about the ocean, about its physics, biogeochemistry, ecosystems, and acoustics, from turbulence to large-scales (Section 1). Usually, ocean science observation campaigns are designed based on scientific objectives and specific questions to be answered. As schematized in Figure 3, observations are to be collected at a fixed time or over some period of time, often referred to as the sampling period. The scientists then use these observations to best estimate something at some fixed time or over some period of time. It is therefore essential to plan and predict the ideal or optimal observations to be made. Sampling questions that are commonly asked include the following: (i) What are the most informative sampling paths, or locations and times, at which measurements should be made? (ii) Which variables or set of variables should be measured, considering the sensor constraints and costs? (iii) Once some measurements are made, should they influence the subsequent sampling and how should they? (iv) Can the known nonlinear and non-Gaussian properties of the dynamics be utilized in the optimal sampling design? Next, we first discuss concepts and overview prior results in optimal adaptive sampling. We then utilize differential equations and information theory to address these questions.

i. Concepts and prior results. Observation data can be utilized on their own, or combined with additional prior knowledge including conservation laws and model equations. The latter usage can take various forms, as summarized on Figure 3 and illustrated in Section 3c. Observations can be integrated into a model by a data assimilation technique to improve

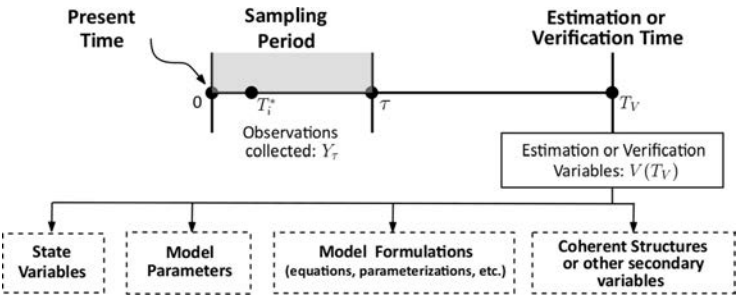

Figure 3. Schematic of the problem statement for adaptive sampling. The aim is to predict the observations Y_τ to be collected over the sampling period τ that are most informative about specific to-be-estimated/verification variables, $V(T_V)$. These verification variables might consist of state variables or fields, model parameters, model formulations (equations, parameterizations, etc.), or secondary variables such as energy or coherent structures. In the schematic, only a single future fixed verification time T_V is sketched, but the estimation time(s) can be in the past or cover a period of time, e.g., the whole sampling period. Also, T_i^* is the optimal arrival time as in Figure 1.

state-variable estimates and field predictions. They can also be employed to infer model parameters. They can be utilized to estimate secondary variables such as energy, enstrophy, spiciness, or even Lagrangian properties and coherent structures of the flow. Finally, they can be used to incubate, test, or improve a model formulation itself, i.e., the model equations and parametrizations, by human research or machine learning. However, not all data are equally informative. On one hand, we need a criterion to evaluate the information content of a set of observations for a particular purpose. On the other, we cannot measure everything we wish to measure due to the limited sensor and instrumentation capability and the constrained platforms mobility. Therefore, given limited platforms and sensors at our disposal and the various quantities of interest to be estimated, the goal is to plan the maneuvers of the observing system optimally such that the observations it collects are the most informative about the scientific objectives. We refer to this automated process in our present larger sense including all applications schematized on Figure 3 as "adaptive sampling" (Lermusiaux 2007; Lermusiaux et al. 2016; Lolla 2016). We note that other definitions of adaptive sampling are more restrictive and emphasize collecting only the data that best improve model forecasts.

The task of adaptive sampling can be divided into three parts: identifying the most informative data (types, locations, and times), planning feasible paths, and integrating results from the previous two. The path-planning part serves two purposes. First, it determines the reachable regions of the platforms that limit the set of candidate measurements that can be made. Then, after the most informative data are determined, the path-planning methodology provides maneuver commands (e.g., headings) to the platforms so that they move along the optimal paths to collect the desired data. To select the most informative data, the

key component is a criterion to evaluate the information content predicted to be contained in a set of observations to be made, with respect to the quantities of interest. Because each measurement will change our prediction of the dynamic ocean environment and the expected information content in a later candidate observation, the planned paths and the computed information content should be updated accordingly, as soon as observation data are collected.

Reviews on previous research on ocean-adaptive sampling are provided in Robinson and Glenn (1999) Leonard et al. (2007), Lermusiaux (2007), Roy et al. (2007), and Paley, Zhang, and Leonard (2008) and the references cited therein. Prior results do not address all of the above and the contributions fall into two main categories. One category is based on some local linearization of the system dynamics. One common approach in this category is the adjoint method for sensitivity analysis (Daescu and Navon 2004; Bergot et al. 1999; Baker and Daley 2000), which uses the gradient of the verification variables with respect to the candidate observations to evaluate how informative these observations are. Another approach is to find the optimal perturbations contributing to the leading singular vectors of the covariance matrix of the verification variables and relate these optimal perturbations to optimal observations (Ehrendorfer and Tribbia 1997; Palmer et al. 1998; Buizza and Montani 1999). Choi and How (2010) used the concept of mutual information to evaluate the information content in candidate observations and compared two forms (filter form and smoother form) of schemes for mutual information-based adaptive sampling, but again they focused exclusively on linear or linearized dynamics.

The other category of results seeks to avoid the linearization of the dynamics. One approach is the breeding method (Toth and Kalnay 1997; Lorenz and Emanuel 1998; Carrassi et al. 2007), which evolves ensembles under the nonlinear dynamics and identify the directions along which the perturbation grows the fastest. Another approach is the ensemble transform Kalman filter (Bishop, Etherton, and Majumdar 2001), which is based on an ensemble Kalman filter (EnKF) and uses an ensemble to evolve the dynamics, to assimilate observation data, and to quantify the effects of candidate observations on the forecast error covariance, all without changing the ensemble. A similar approach is the error subspace scheme (Lermusiaux 1999a; Wang et al. 2009), which keeps track of the time-evolution of a dominant low-rank approximation to the error covariance matrix using nonlinear ensembles and re-runs the ensemble after each candidate assimilation. Other approaches in this category include mixed-integer programming approaches (Yilmaz et al. 2008), potential functions (Munafò et al. 2011), genetic algorithms (Heaney et al. 2007; Frolov, Garau, and Bellingham 2014; Heaney et al. 2016), etc. Note that all of the above adopt a Gaussian approximation of the distributions of all the involved state variables, which neglects the non-Gaussian features of the statistics.

ii. Adaptive sampling with differential equations and information theory. To address the challenges in adaptive sampling for ocean applications, we recently integrated several newly-developed theory and methodologies for uncertainty quantification, Bayesian data

assimilation and information theory. The result is a novel and rigorous framework for predicting the most informative observations (Lolla 2016).

The dynamically orthogonal (DO) equations (Sapsis and Lermusiaux 2009; Ueckermann, Lermusiaux, and Sapsis 2013; Feppon and Lermusiaux 2018a, b) perform an optimal dimension reduction and quantify uncertainty propagation under nonlinear dynamics. The DO methodology uses a truncated dynamic K-L (Karhunen–Loeve)-like expansion to approximate the time-dependent random vector fields:

$$\boldsymbol{u}(\boldsymbol{x}, t; \omega) \approx \bar{\boldsymbol{u}}(\boldsymbol{x}, t) + \sum_{i=1}^{S} \phi_i(t; \omega)\boldsymbol{u}_i(\boldsymbol{x}, t). \tag{8}$$

The DO modes $\boldsymbol{u}_i$'s (instantaneous and dynamic, instead of Empirical, Orthogonal Functions) are orthonormal under a specified inner product and the DO coefficients ϕ_i's have zero mean and are commonly represented by Monte Carlo samples. This expansion captures the dominant uncertainty of $\boldsymbol{u}(\boldsymbol{x}, t; \omega)$ living in a time-evolving S-dimensional subspace spanned by the $\boldsymbol{u}_i(\boldsymbol{x}, t)$'s. By a Galerkin projection approach, dynamical equations of the mean $\bar{\boldsymbol{u}}$, DO modes $\boldsymbol{u}_i$'s, and DO coefficients ϕ_i's are obtained and are used to track the time evolution of the stochastic $\boldsymbol{u}(\boldsymbol{x}, t; \omega)$ under the governing dynamics.

Furthermore, the Gaussian mixture model (GMM)-DO filter (Sondergaard and Lermusiaux 2013a, b) and smoother (Lolla and Lermusiaux 2017a, b) is used to capture non-Gaussian statistics in the reduced DO subspace for data assimilation. The PDF (probability density function) of a GMM random vector $\boldsymbol{\phi} \sim \text{GMM}(\pi_{1:M}, \boldsymbol{\mu}_{1:M}, \boldsymbol{\Sigma}_{1:M})$ is a linear combination of PDFs of multivariate Gaussian distributions:

$$p_{\boldsymbol{\phi}}(\boldsymbol{x}) = \sum_{i=1}^{M} \pi_i \mathcal{N}(\boldsymbol{x}; \boldsymbol{\mu}_i, \boldsymbol{\Sigma}_i), \qquad \pi_i \geq 0, \quad \sum_{i=1}^{M} \pi_i = 1. \tag{9}$$

The flexibility of estimating the optimal number of components M (e.g., by Bayes information criterion) and fitting parameters of the various Gaussian components to samples (e.g., by the expectation–maximization algorithm) allows capturing the multi modal and asymmetric features of the underlying non-Gaussian distributions. The Bayesian paradigm is adopted throughout the framework to incorporate information from disparate sources sequentially in a principled way.

For information content evaluation, we follow the information-theoretic approach and used mutual information (Cover and Thomas 1991), which takes into account non-Gaussianity and readily generalizes to multivariate scenarios. The mutual information between two continuous random vectors $\boldsymbol{\phi}$ and $\boldsymbol{\psi}$ with joint PDF $p_{\boldsymbol{\phi}\boldsymbol{\psi}}(\boldsymbol{x}, \boldsymbol{y})$ is defined as

$$I(\boldsymbol{\phi}; \boldsymbol{\psi}) = \int_{\mathbb{R}^{d_1} \times \mathbb{R}^{d_2}} p_{\boldsymbol{\phi}\boldsymbol{\psi}}(\boldsymbol{x}, \boldsymbol{y}) \log \frac{p_{\boldsymbol{\phi}\boldsymbol{\psi}}(\boldsymbol{x}, \boldsymbol{y})}{p_{\boldsymbol{\phi}}(\boldsymbol{x}) p_{\boldsymbol{\psi}}(\boldsymbol{y})} \mathrm{d}\boldsymbol{x}\mathrm{d}\boldsymbol{y}, \tag{10}$$

where d_1 and d_2 are the dimensions of $\boldsymbol{\phi}$ and $\boldsymbol{\psi}$, respectively, and $p_{\boldsymbol{\phi}}(\boldsymbol{x})$ and $p_{\boldsymbol{\psi}}(\boldsymbol{y})$ are the marginals. Mutual information is always nonnegative and it vanishes if and only if the two random vectors involved are statistically independent. The mutual information characterizes how much "common" information the two random vectors share, which is a good indicator of how informative is one random vector about the other. In the GMM-DO framework adopted here, to compute such mutual information, the joint PDF $p_{\boldsymbol{\phi}\boldsymbol{\psi}}$ is approximated using a GMM and a Monte Carlo method is used to numerically compute the integral (10) in the DO subspace, as

$$I(\boldsymbol{\phi};\boldsymbol{\psi}) \approx \frac{1}{N_{\mathrm{MC}}} \sum_{i=1}^{N_{\mathrm{MC}}} \log \frac{\hat{p}_{\boldsymbol{\phi}\boldsymbol{\psi}}\left(\hat{\boldsymbol{\phi}}^{(i)}, \hat{\boldsymbol{\psi}}^{(i)}\right)}{\hat{p}_{\boldsymbol{\phi}}\left(\hat{\boldsymbol{\phi}}^{(i)}\right) \hat{p}_{\boldsymbol{\psi}}\left(\hat{\boldsymbol{\psi}}^{(i)}\right)}, \tag{11}$$

where the $\hat{\boldsymbol{\phi}}^{(i)}$'s and $\hat{\boldsymbol{\psi}}^{(i)}$'s are N_{MC} samples drawn from the GMM approximation $\hat{p}_{\boldsymbol{\phi}\boldsymbol{\psi}}$. Because an affine transformation (i.e. $\boldsymbol{f}(\boldsymbol{x}) = \boldsymbol{A}\boldsymbol{x} + \boldsymbol{b}$) of a GMM random vector is still a GMM random vector, we can analytically compute the GMM approximation for most common quantities of interest from the GMM approximation fitted to the DO coefficients. This is because the DO expansion (8) is an affine transformation and many quantities of interest are related to the state vector $\boldsymbol{u}$ by an affine transformation.

For reachability region computation and optimal navigation, the rigorous reachability and path planning methodologies based on level-set equations is employed (Section 2a). Finally, an exact dynamic programming scheme is employed to formulate a sequential procedure to integrate the various components, so that whenever the observations are incorporated to update the knowledge of the dynamic environment, the future sampling strategies are adjusted and planned accordingly (Lolla 2016).

c. Teaming machines and scientists: Expert ALPS systems

The reachability, path planning, and adaptive sampling methods and equations outlined in Sections 2a and b constitute fundamental knowledge that provides quantitative predictions and allows inferences to be made about the ocean. In theory and as illustrated in Section 3, they should be utilized by ALPS for autonomous decision making and task completion for optimal ocean observation. If costs were not an issue, sea experiments could even be repeated as needed to formally crystallize advances in the science of autonomy.

In machine learning and artificial intelligence, an expert system is a system that has computational capabilities and that emulates the decision-making ability of humans with expert knowledge (Jackson 1998; Russell and Norvig 2009). The expert knowledge of an ocean observing researcher consists of the fundamental conservation laws and quantitative models of ocean science, in the forms of governing equations, dominant balances, statistical information, parameter values, and many other mathematical or back-of-the-envelope relations. It also consists of varied engineering expertise in ocean platforms and sensors. This vast prior knowledge is a major difference with the present sociotechnical applications of big

data and machine learning (e.g., Pentland 2014). In these applications, very little is known a priori, at least not in the form of numerical or mathematical relations. An ALPS system, on the other hand, is not an uninformed learner: definitely not if it is guided now-and-then by ocean scientists, but not even if it is fully autonomous because it commonly stores and uses prior information. We note that, in the former case, the observing machines and humans form a networked system (Curtin and Bellingham 2009) and such human-machine collaborative teaming is likely to become a norm in the future. The ideal autonomous ocean observing system is thus a true "*expert system*". Learning for such observing experts should be optimized: when entering a library, we often explore random books in a lawnmower pattern, but usually, we also have some focus in mind. We don't read all of the books but, mostly, books we are interested in.

Many ocean ship surveys have consisted of vertical sections and lawnmower sampling patterns, mainly because ocean researchers wanted such estimates (e.g., measure the transport through a strait) or because not all of what researchers knew was utilized in an optimal expert way. Even for pure exploration, some exploitation with path planning or adaptive sampling becomes useful (e.g., Smith et al. 2011; Graham and Cortés 2012; Heaney et al. 2016). As mentioned earlier, as soon as observations are collected and analyzed, knowledge is acquired and plans should be improved (e.g., Das et al. 2015).

It is clear that quantitative methods and fundamental equations discussed in prior sections provide a basis for the inference engine and knowledge base of expert observing systems. However, ALPS located far away from ships and/or far beneath the sea surface cannot sustainably exchange instructions and commands with scientists and cannot store all knowledge nor run complex models for a long time. Consequently, for the use of vehicles in missions involving the exploration of remote ocean areas, vehicles are on their own. Storing not all but only the optimal prior-to-mission knowledge is then crucial. Indeed, AUVs operating in remote environments must not only have the capability to sense their environment, but also be able to react to changing conditions (e.g., unexpected currents, turbulence, wakes, or obstacles). Ideally, they should be capable of re-planning paths (optimal time, energy, etc.) and of adaptive sampling onboard. They can then reach the locations needed to conduct optimal data gathering as quickly as possible, or conserving as much energy as possible (or both).

The past two decades have been witness to significant progress in autonomous remote sensing, machine learning, mission planning, and adaptive control, as reviewed by Jiménez et al. (2012) and Bellingham and Rajan (2007). Several software architectures for ocean sensing and automated mission planning have been developed. They can utilize survey error metrics accounting for under-sampling and environmental changes (Willcox et al. 2001), integration of the deliberation and reaction process (McGann et al. 2009), and networked approaches for large groups of (possibly collaborating) vehicles with disparate sensing and communications capabilities (Benjamin et al. 2010). Sonnenburg and Woolsey (2013) also learned experimentally-identified models for rigid hull inflatable boats. Yoo and Kim (2016) used reinforcement learning algorithms with ocean effects for AUV path planning.

In both unknown and known environments, the operational characteristics of vehicles can be learned onboard using data-driven machine learning. Regression analysis, time-series analysis, neural networks, supervised learning, and clustering are then applied to the mission data. After time-optimal path planning exercises (see Section 3a), such techniques were used to investigate the at-sea operational characteristics of AUVs, focusing on vehicle-speed-to-power relationships (Edwards et al. 2017).

3. Applications

We now present several recent at-sea campaigns and operational simulations that showcase capabilities and benefits of utilizing rigorous reachability, path planning, adaptive sampling, and machine learning schemes for autonomous observing systems. Our theory and software for real-time path planning is first employed for racing two identical REMUS 600 AUVs in the Buzzards Bay and Vineyard Sound region (Section 3a). We then exemplify deterministic and probabilistic three-dimensional reachability and path forecasts issued daily for gliders and floats operating for two months in the northern Arabian Sea (Section 3b). Novel Bayesian adaptive sampling for hypothesis testing and optimal learning is then illustrated (Section 3c). Specifically, computing machines forecast the observations that are most informative to estimate the accuracy of model formulations, the values of ecosystem parameters and dynamical fields, and the presence of Lagrangian Coherent Structures in the flow (Section 3c).

In all applications, the MIT Multidisciplinary Simulation Estimation and Assimilation System (MSEAS) is employed for flow and ocean simulations. Its modeling capabilities include implicit two-way nesting for realistic tidal-to-mesoscale dynamics with hydrostatic primitive equations (PEs) and a nonlinear free-surface (Haley and Lermusiaux 2010; Leslie et al. 2010; Haley, Agarwal, and Lermusiaux 2015) as well as a finite-volume code for nonhydrostatic dynamics and incubation of new methods (Ueckermann and Lermusiaux 2012).

a. At sea time-optimal path planning

To demonstrate our exact time-optimal planning theory and test its applicability for real-time operations using our software, we undertook multiple sea exercises with one AUV on 21 October 2016 and with two AUVs on 6 December 2016. In all cases, the AUVs following time-optimal path predictions behaved as forecast and won the races. Here, we present results for one of our 2-AUV races.

That 2-AUV race experiment was conducted in the Vineyard Sound region (Fig. 4a). Two near-identical REMUS 600 AUVs with the exact same operational settings (e.g., engine RPM, payload, etc.) were released from the same location and piloted to the same target, maintaining a 3-m depth and an engine RPM corresponding to a nominal speed of 3 knots (a common AUV speed). One AUV followed our forecast time-optimal (but longer) path and the other AUV the shortest distance path. Sensors on the AUVs recorded oceanographic

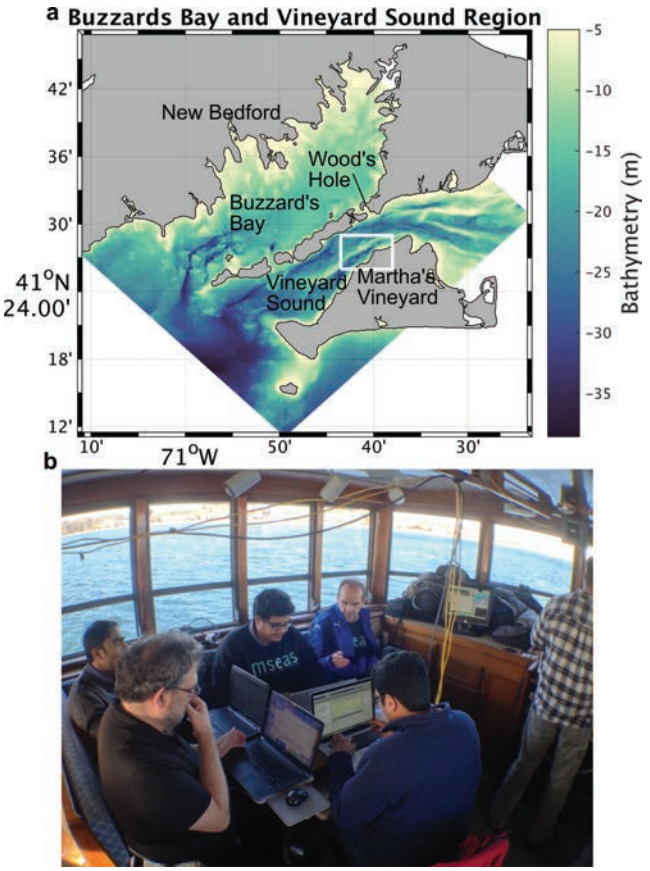

Figure 4. We demonstrated our path-planning equations and software during real-time sea exercises in the Buzzards Bay and Vineyard Sound region. **(a)** Bathymetry of the computational domain. The white box is the region magnified in Figure 5. **(b)** For all sea experiments, we computed the time-optimal reachability fronts and paths onboard the R/V Discovery in less than one minute on laptops.

and operational data along the paths. The headings for both the vehicles were forecast using our planning equations and software ran on laptops on-board the R/V Discovery (Fig. 4b). Each reachability and path computation took less than a minute. The time-optimal path used the MSEAS current forecasts in its planning PDEs. The shortest-distance path was computed exactly using the same level-set equations but with currents set to zero. As a result, both paths respected all operational constraints (e.g., avoiding too shallow regions, safety constraints, etc.) because these constraints are directly included within the level-set integration (equations 3 and 5; Lolla et al. 2014a,b, 2015). For example, the too-shallow shoals in the Middle Ground region were avoided.

To predict the local circulation, we employed the MSEAS PE ocean modeling system, using a domain with 100-m horizontal resolution and 12 vertical levels (Fig 4a). Tides from the OSU TOPEX/Poseidon Global Tidal Inverse Solution TPXO (Egbert and Erofeeva 2002, 2013) were reprocessed for the higher resolution bathymetry, nonlinear bottom drag, and observational data using our inversion procedures (nonlinear extension of Logutov and Lermusiaux (2008)). Our currents forecast was for 3 days starting from 00 Z, 04 December 2016 using the latest 5-km and 1-hour-resolution forecasts from the Weather Research and Forecasting (WRF) simulations at National Centers for Environmental Prediction (NCEP) (NCEP 2017) available at 12 Z, 05 Dec 2016.

The race occurred off the northwest coast of Martha's Vineyard along the Middle Ground starting at 18:15 Z and continued until 20:20 Z. Early in the day, winds were southward but began to change direction to become southwestward at 10–11 knots by 18 Z. Thereafter, the winds maintained strength (11–13 knots) until 21 Z. The circulation in the Vineyard Sound region is strongly influenced by M2 tides with complex and rapid modulations of tidal phases and currents by the coastlines, semi-enclosed water bodies, and complex bathymetry including sand bars and rises such as Middle Ground just northwest of Martha's Vineyard. The wind-forcing and density-driven flows modify this surface intensified tidal flow. From 17 to 19 Z, the tides built a strong flow to the northeast strengthening to 60–110 cm/s. Shoals in Vineyard Sound introduced smaller scale features and rips, both north of West Chop and in the Middle Ground to the east of Lamberts Cove. Over the next hour, the tides began to weaken, becoming slack and reversing direction by 22 Z.

Figure 5a shows six snapshots with the progressing paths of the two vehicles, from the start of the experiment until when the time-optimal AUV reached the target. From the first three snapshots, between 18:15 and 18:55 Z, the time-optimal AUV crossed the strong opposing jet (with flows 100 cm/s) and reached a region with weaker opposing flows ($\sim$70 cm/s) to continue its path. On the other hand, the shortest distance AUV got caught in opposing flows of up to 110 cm/s and had to abort its mission temporarily at 18:37 Z. This AUV was restarted by 18:52 Z and continued its mission plan. From 18:55 to 19:35 Z, the time-optimal AUV traveled in regions with weaker opposing flow than that of the shortest distance AUV. The flows in the Middle Ground region started to weaken overall by 19:35 Z and the time-optimal AUV completed its mission at 19:52 Z. The shortest distance AUV was allowed to continue to account for the 15 minutes lost in restarting. Then, at 20:09 Z, when it was apparent that the shortest-distance AUV was going to arrive much later than the forecast time-optimal AUV, the mission was aborted to save time for further experiments. At 20:09 Z, the straight-line AUV was still about 1 km away from the target. We then estimated the total travel-time from start to finish for the two vehicles by correcting for the remaining distance and restart (Subramani et al. 2017). Even if we discount the time lost by the restart of the shortest-distance AUV, the forecast time-optimal AUV took 96.12 mins, about 15% faster than the shortest-distance one, which took 110.72 mins. Moreover, both the time optimal and shortest distance AUVs were operated at 525 rpm and achieved average nominal speeds of 153.34 cm/s and 148.08 cm/s, respectively (very close to the

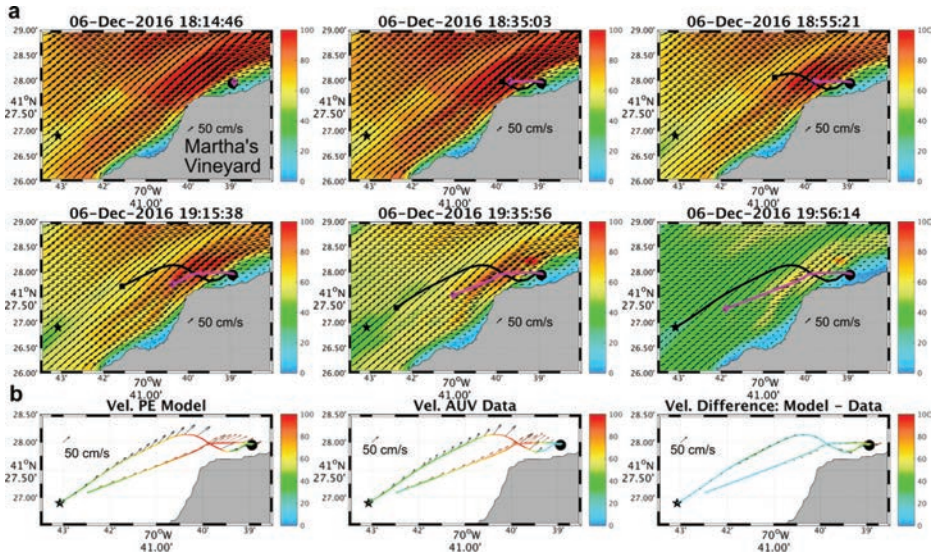

Figure 5. **(a)** Sequence of six equally spaced snapshots, all at 3 m depth, from the start location of the two AUVs until the time-optimal AUV reached the target. The magnitude of forecast currents (cm/s) overlaid by velocity vectors is shown in the background. The time-optimal AUV path until the time of each snapshot is shown by a solid black line with its current position by black square marker. The shortest distance AUV path is similarly shown by a solid magenta line and a magenta diamond marker. When the time-optimal AUV reached the target, the shortest distance AUV was still about 2 km away. **(b)** Left panel: magnitude and vectors of current forecasts at 3 m depth, along the two AUV tracks, at the times at which the AUVs were at those locations. Middle panel: currents as measured by the acoustic Doppler current profiler (ADCP) on board the respective AUVs. Right panel: difference between our model predictions and the measured data. The Multidisciplinary Simulation Estimation and Assimilation System primitive equation (MSEAS PE) could predict the magnitude and directions accurately.

RPM setting corresponding to 3 knots). Hence, the time-optimal AUV clocked an average effective speed of 146.06 cm/s compared with the shortest-distance AUV averaged speed of only 116.93 cm/s due to experiencing stronger opposing flows.

In Figure 5b, we compare the instantaneous local currents along the path of the REMUS 600 as predicted by our PE modeling system and as measured by the on board acoustic Doppler current profiler (ADCP). Specifically, we show the PE forecasts of the current magnitude and subsampled vectors along the AUV path (left panel), the data measured by the REMUS 600 AUV (middle panel), and the difference between the two (right panel). We see that our modeling system could predict the direction and magnitude of the currents (beating persistence by more than 100% and a tidal model by more than 50%, not shown). We note that in such shallow regions and with very limited data, it was difficult to model and

predict currents accurately. Hence, this result is encouraging for the future of integrating coastal ocean predictions with rigorous optimal path planning.

b. Probabilistic Eulerian-Lagrangian reachability in the Northern Arabian Sea

The Arabian Sea is characterized by strong western boundary currents, a large reservoir of internal energy in the mixed-layer with complex (sub)mesoscale fields, and strong seasonally-reversing monsoon winds that can reserve boundary currents and circulation features (e.g., Schott and McCreary 2001). The Office of Naval Research-funded NASCar program is investigating this dynamics using a variety of ALPS systems (Centurioni et al. 2017a, b). During February–April 2017 (Lermusiaux et al. 2017b), we forecasted the following: (i) the regional high-resolution ocean fields and their probability, using error subspace statistical estimation (ESSE) (Lermusiaux and Robinson 1999; Lermusiaux 1999b, 2006, 2007); (ii) the reachable sets, reachability fronts, and time-optimal paths of underwater gliders and floats; (iii) the uncertainty of such reachability fields and optimal paths. Specifically, we forecasted the reachability fronts of two SeaGliders (SG133 and SG137) and the dynamic probability of reachable points of an Air-Launched Autonomous Micro Observer (ALAMO) float (9103). The SeaGliders were navigating in bow-tie pattern to track the ALAMO float (Centurioni et al. 2017a, b). The float was profiling to about 300 m in every 2 hours and the SeaGliders were diving to 1,000 m in 4–5 hours.

i. Ensemble ocean forecasts. The MIT MSEAS-PE modeling system was used in real-time to issue 3-day ensemble ocean forecasts daily. The NASCar modeling domain (Figure 6a) in the northern Arabian Sea had a 1/60° horizontal resolution and 70 vertical levels with optimized level depths (e.g. higher resolution near the surface or large vertical derivatives). This resolution was needed to develop and maintain complex layered features (not shown). The bathymetry was obtained from the 15 arc-seconds SRMT15 data (Smith and Sandwell 1997). The initial conditions were downscaled from 1/12° Hybrid Coordinate Ocean Model (HYCOM) analyses (Cummings and Smedstad 2013) via optimization for our higher resolution coastlines and bathymetry (Haley, Agarwal, and Lermusiaux 2015). Tidal forcing were computed from the high-resolution TPXO8-Atlas from OSU (Egbert and Erofeeva 2002, 2013), by reprocessing for our higher resolution bathymetry/coastline and quadratic bottom drag. The atmospheric fields consisted of the wind stresses and surface freshwater flux from 1/4° NCEP GFS 1-hourly forecasts (Env. Mod. Center, 2003) and the net heat flux from 1/2° NAVGEM 3-hourly forecasts (Hogan et al. 2014).

To predict uncertainties, 50-member ensemble forecasts were issued daily using ESSE, from mid-March to April. To initialize multiscale ensembles (Lermusiaux, Anderson, and Lozano 2000; Lermusiaux 2002, 2007), historical CTD (conductivity, temperature, depth) synoptic data for the months of January, February, and March were used to create vertical EOFs (empirical orthogonal function) for temperature (T) and salinity (S). The EOFs were

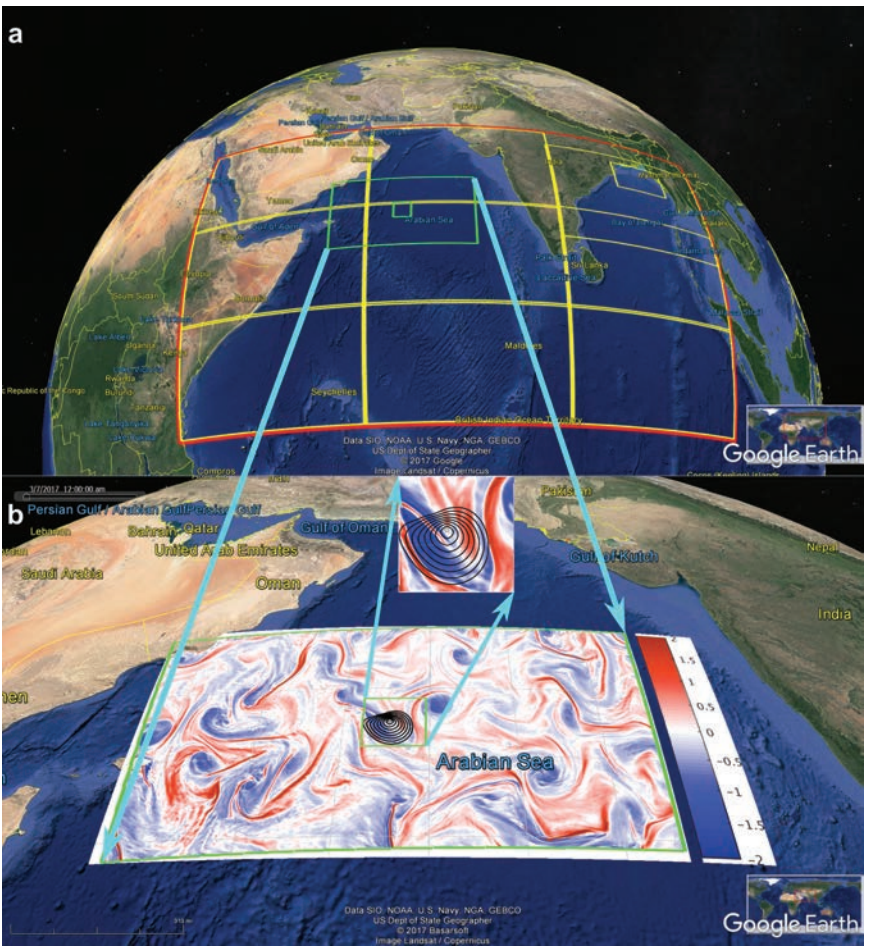

Figure 6. **(a)** MIT MSEAS multiresolution computational domains in the northern Indian Ocean. The domain bounded by the green outer box (53.66–69.18E; 9.38–17.83N) is the main domain used for real-time forecasts to support Northern Arabian Sea Circulation-Autonomous Research (NASCar) operations. **(b)** Three-day forecast of the vorticity field at 2 m, issued by the MSEAS-PE for 7 March 2017 00Z (middle time for the 5–9 March 2017 forecast period for SG137). A smaller moving domain (green inner box) surrounds the initial position of SG137 on 5 March 2017 00Z. The black contours are four days of reachability front forecasts, at 12 hour intervals (12h to 96h forecasts). The reachability front is the boundary of the largest set (the reachable set) that the glider can reach within that duration. It was forecast by integrating its exact governing level-set time–optimal PDE.

combined with an eigendecomposition of a horizontal correlation matrix based on a Mexican hat function of 25-km decay-scale and 75-km zero-crossing, to construct 3-dimensional T and S perturbations. These T and S perturbations were used to generate velocity perturbations in accordance with PE balance. Fifty such ensemble members were created and the MSEAS-PE model was integrated in time for each of them, using also stochastic error models for tides and atmospheric fields.

ii. Glider reachability forecasts. For the operational guidance of sea-gliders SG133 and SG137, their 4-day reachability forecasts were issued daily. These gliders are piloted in a yo-yo pattern performing 1,000 m dives in 4 to 5 hours. Accordingly, the level-set equation (5) was solved with our 0–1,000 m depth integrated ocean forecasts (Lolla et al. 2014a). In Figure 6b, we illustrate a 2-m mesoscale vorticity forecast and a glider reachability forecast. In Figure 7, four forecasts for SG133 and SG137 issued in the second half of March 2017 are shown. In each panel of Figure 7, the reported location of the glider at the beginning of the forecast window is shown as a gray point and the reachability fronts at every 12 h by black contour lines overlaid on a forecast of the 48-h depth–averaged currents. The area within the reachability front can be visited by the gliders whereas the area outside cannot (Section 2a). Overall, the growth and shape of the reachability fronts are set by the local circulations.

For the period 18 to 22 March (Fig. 7a and b), for SG133, the forecast currents are as follows: westward to its west, northwest, and north; southwestward to its northeast and east, and finally northwestward to its southeast, south and southwest. Further to the east of SG133, forecast currents are southward. As such, the reachability front grows to the west, northwest, and southeast. There is less growth to the south owing to the stronger opposing flows of about 15 cm/s. For SG137, currents are northwestward in a 270° arc from its east to north, and southwestward in its northeast. Similarly to SG133, further to the east of SG137, the currents are southward. Hence, the reachability fronts grow more to the northwest due to supporting flows and less to the south due to opposing flows. For later times, the reachability front grows farther to the east as the opposing flows are weaker there. During 21 to 25 March (Fig. 7c and d), SG133 is in a strong southeastward forecast flow and SG137 is to the west of it. As such, the reachability fronts of SG133 grow more to the southeast than those of SG137. During 23 to 27 March (Fig. 7e and f), both gliders SG133 and SG137 are in the strong southeastward flow proper. Hence, their reachability fronts forecast grow in that direction. During 26 to 30 March (Fig. 7g and h), current remain southeastward but curve towards the east (south of the moving domain). On 26 March, SG137 is located to the southeast of SG133. SG133 is more in the southeastward flow than SG137, and hence the formers reachability fronts grow faster than the latters. Finally, the local shape of the reachability fronts is governed by the mesoscale flows and shear. For example, the kidney bean shape in the forecast reachability fronts (prominent for the 96h forecasts) in Figure 7c and e–h is due to the focal flow shear.

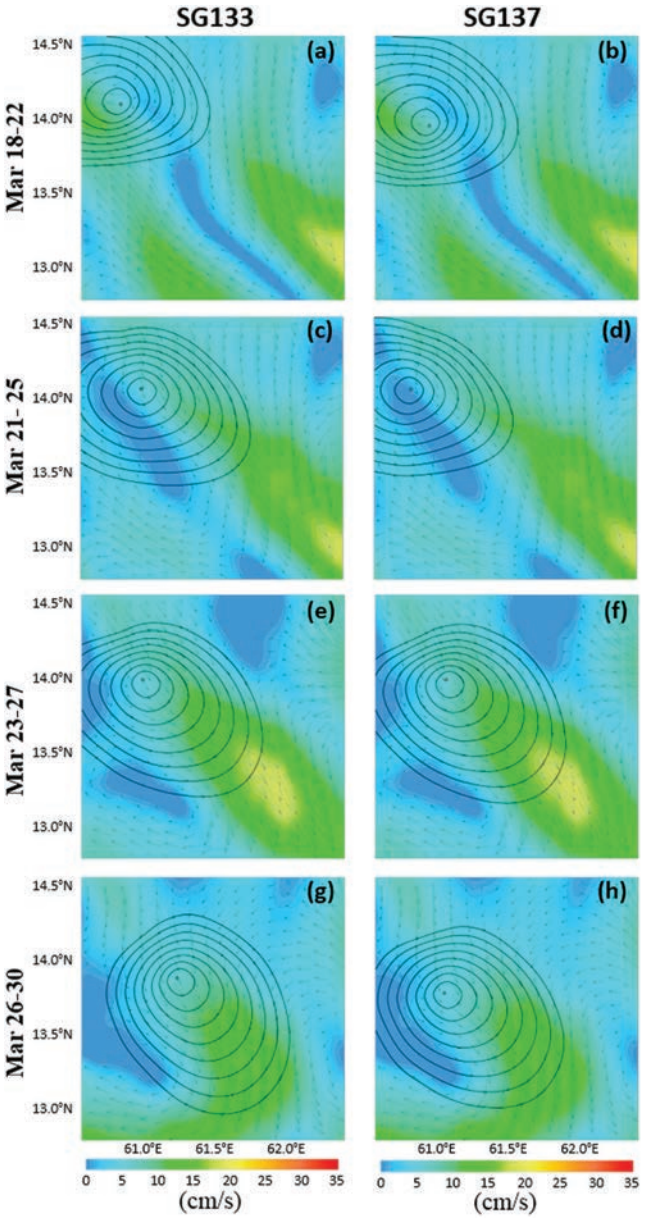

Figure 7. Reachability front forecasts for SeaGliders SG133 and SG137 for 18–22 March (a, b); 21–25 March (c, d); 23–27 March (e, f); and, 26–30 March (g, h) 2017. The locations of the glider at the beginning of the forecast window are shown as gray points and the reachability fronts at every 12 h (12h-96h) by black contour lines. The background is a color plot of the 0–1000-m depth averaged flow magnitude (cm/s) overlaid with velocity vectors.

iii. ALAMO float forecasts. Forecasts for the 4-day future positions of ALAMO floats were also issued daily. To account for uncertainties in the initial float positions and initial flows around it, we first advected a dynamic set of possible reachable positions, starting from a small circle around the latest known positions of the floats. The reachable sets, then, estimate the region outside of which the likelihood of finding the float is small. These sets were forecast from the latest known positions of each float and issued in 12-hour intervals.

Fig. 8 shows six examples of such forecasts issued on 18, 19, 21, 23, 25, and 26 March. They are overlaid on the 0–300 m–averaged 48-h (midpoint of the forecast window) velocity forecast magnitude and vectors. Each forecast is accompanied by a plot of the real track of the float during the forecast horizon. On 18 March (Fig. 8a), the float is in a region of low velocity with east-west shears from adjacent stronger currents. The forecast reachable set initially advects westward but then elongates (due to the shear), both eastward and westward. This was consistent with the actual float, which initially moved westward but then reversed and advected eastward. In the forecast issued on 19 March (Fig. 8b), the southeastward strong flow northeast of the float increases. As such, the float is forecast to advect southward, with the eastern edge of the reachable set moving southeast. On 21 March (Fig. 8c), the float is at the edge between weak and strong southeast flows. Hence, the eastern edge of the reachable set grows farther south than the western edge. In the above three sets, the shear in the forecast flows stretches the reachable set thereby elongating the initial circle to ellipse shapes. The real float track (Figs. 8a, b, and c) is consistent with forecasts and improves with the strength of the flow near the float. In the 23, 25, and 26 March forecasts (Figs. 8d, e, and f), the float is in the strong flow proper. It is thus forecast to move faster, which again agrees with the real float tracks (Figs. 8d, e, and f).

The skill was mostly governed and limited by the accuracy of the larger time-dependent mesoscale flow. To account for its complete dynamic uncertainty, we employed ESSE ensembles to predict the dynamic set of reachable positions for each ensemble member. A rigorous probability field of reachable float positions is then obtained by normalizing by area the union of each ensemble's set of reachable positions. This probabilistic reachable set field forecast for the ALAMO float issued on 26 March 2017 00Z for the period 26–31 March is depicted in Figure 9. The nine panels show the forecasts every 12 h from 26 March 00Z. The color represents the quantitative probability that a location on the map is in the reachable set for the float. Overlaid on the probability map are 0–300-m averaged current vectors from the central MSEAS forecast and the real track of the float from the 26 March 00Z to the time of the forecast of each panel. These results show that the real float location remained within the probabilistic reachable set forecast (i.e., within the colored region of probable locations).

Similar results were obtained for forecasts on other days (Lermusiaux et al. 2017b). Overall, our Lagrangian probabilistic reachability planning system showed 4-day predictive skill repetitively during the real-time experiment. Such capability allows new evaluation of stochastic ocean forecasts. It is also useful for other applications such as Lagrangian

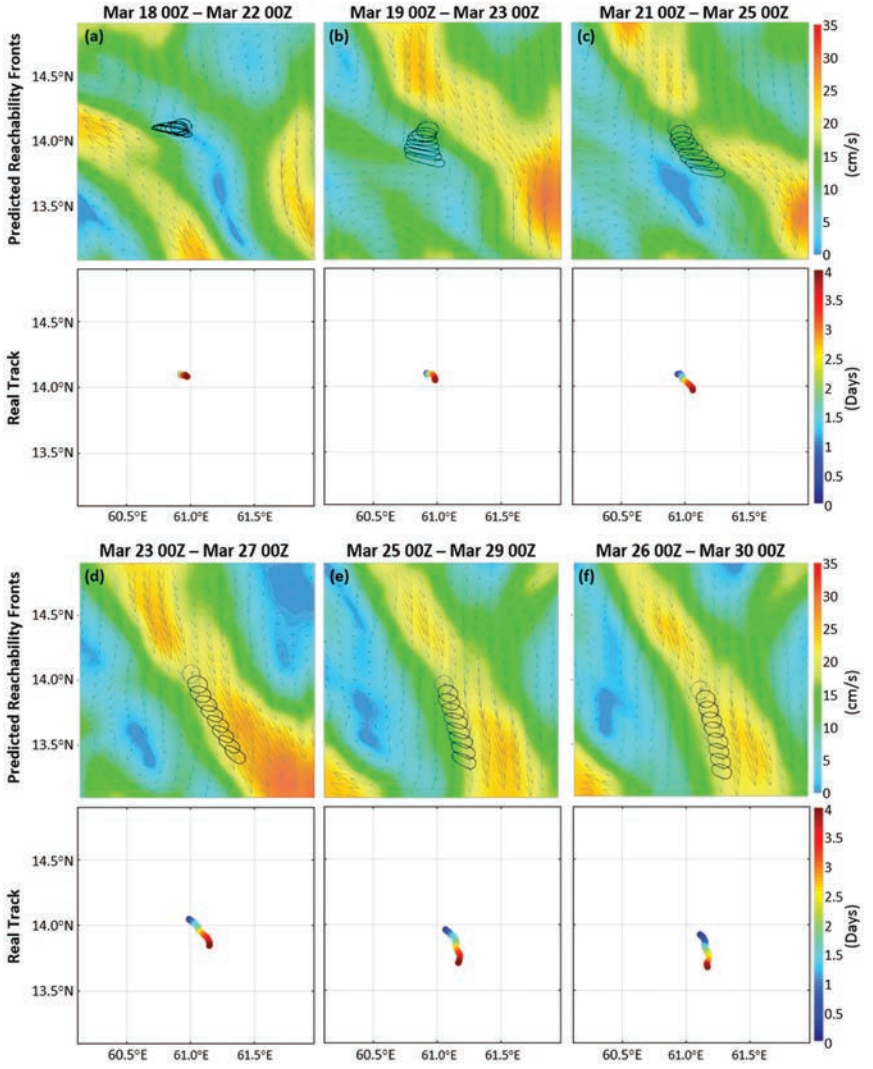

Figure 8. Six sets (a–f) of dynamic reachable set forecasts and the real observed track of the ALAMO Float S/N:9103. In the panels for forecasts show the initial uncertain float position (gray circle) and 12-h forecasts (12–96 h) of the corresponding reachable sets (solid black contour lines). They are overlaid on the 48-h forecasts of the 0–300-m averaged current magnitude (cm/s) and velocity vectors. The real tracks are colored by the number of days since the time at which the forecast was issued. Here, the reachable set is the region outside of which the likelihood of finding the float is small. The forecasts had good skill, mostly governed and limited by the accuracy of the larger mesoscale flow.

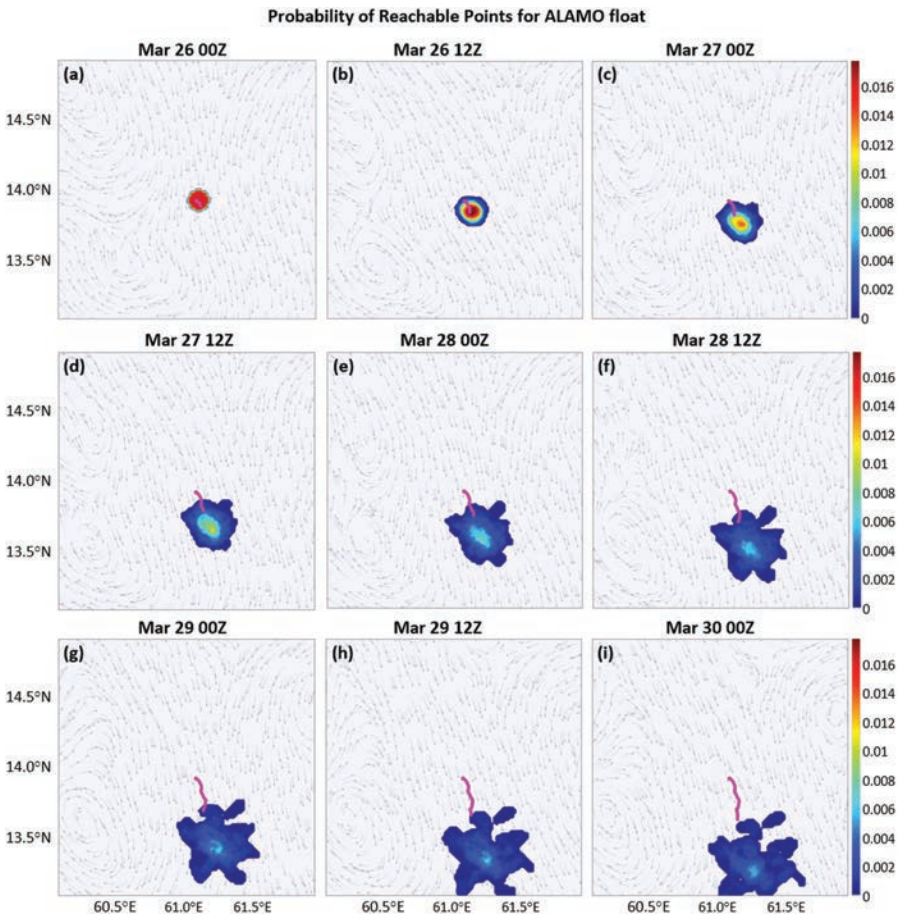

Figure 9. Probabilistic forecast of the dynamic reachable sets for the ALAMO float for every 12 h, issued on 26 March 2017. The colored field is the probability of that location being part of the reachable set. The real observed track of the float from the 26 March 00Z to the time of the forecast of each panel is shown by a solid magenta line. All are overload on the 0–300-m averaged current vectors from the central MSEAS PE forecast.

dynamics studies, float data assimilation, float recovery and safety, and float sampling system optimization.

c. Bayesian adaptive sampling for hypothesis testing and optimal learning

To make full use of the measuring power of all types of platforms in an automatic manner, an adaptive sampling methodology for deploying them wisely is needed. As discussed in Section 2, it should be designed according to the variables to be estimated, to what is

known and not known about the ocean dynamics to be sampled, and to the platforms and sensors capabilities. A critical component of adaptive sampling is how to measure the information contained in different candidate observations to be made. For such information metric, a rigorous choice is to employ mutual information, i.e., the "amount of information" obtained about the estimation variables through the observations. Hence, the goal of adaptive sampling is then to maximize this mutual information over all locations that could be reached by the platforms available. Next, we illustrate these concepts in idealized and realistic ocean scenarios using our general Bayesian adaptive sampling framework (Section 2). Specifically, we predict optimal measurement locations for hypothesis testing and model learning, for estimating parameters and fields, and for revealing Lagrangian coherent structures.

i. Optimal observations for hypothesis testing: Learning model equations. Figure 10 illustrates how mutual information can determine the data ideal for model learning. The underlying dynamics in this application is an idealized bottom gravity current (Özgökmen and Chassignet 2002), where salty water over the top of the plateau on the left flows down the slope, driven by gravity. As shear takes place in the interface between the down-flowing salty water and the ambient quiescent water, an hydraulic head and Kelvin–Helmholtz instabilities are commonly triggered and multiscale flow features are developed. The first and the third panels of Figure 10 show a typical salinity field (unit: psu) of such flow at $T = 10$ min and $T = 60$ min, respectively.

For this machine learning example, our goal is to best infer the slope angle and the magnitude of the initial salinity anomaly over the plateau. Therefore, we (scientists) propose different models that differ in these aspects (e.g., nine models in this example with different combinations of salinity anomaly magnitude and slope angle) and the computing machine is to learn the "right" model from a few sparse salinity measurements in a hierarchical Bayesian manner. Specifically, this is achieved by propagating the uncertainty using the DO equations and assimilating the observations using the GMM-DO filter for each candidate model (see Section 2bii for an outline of these methods) so as to obtain the model likelihoods, and then using in these likelihoods and our prior beliefs over the candidate models into the Bayes formula to compute the posterior beliefs. Note that this is performed sequentially as new data become available over time.

The white dots shown in Figure 10 indicate the 10 observation locations initially picked heuristically by humans, where the salinity is measured. To indicate how this choice could be improved, in the second and the fourth panel, the field of mutual information $I(S(\boldsymbol{x}, t), \mathcal{M})$ between salinity $S(\boldsymbol{x}, t)$ and the model identity $\mathcal{M}$ is shown at time $t = 10$ min and $t = 60$ min. Here, the model identity $\mathcal{M}$ is a discrete random variable that takes its value from the set of candidate models $\{\mathcal{M}_1, \mathcal{M}_2, \ldots\}$, so $\Pr(\mathcal{M} = \mathcal{M}_i)$ is the probability that the i-th model is the true model. Note that $I(S(\boldsymbol{x}, t), \mathcal{M})$ is defined by equation (10) except that the integral with respect to the PDF for $\mathcal{M}$ should be replaced by a summation with respect to the probability mass function. Moreover, $I(S(\boldsymbol{x}, t), \mathcal{M})$ is numerically computed through equation (11).

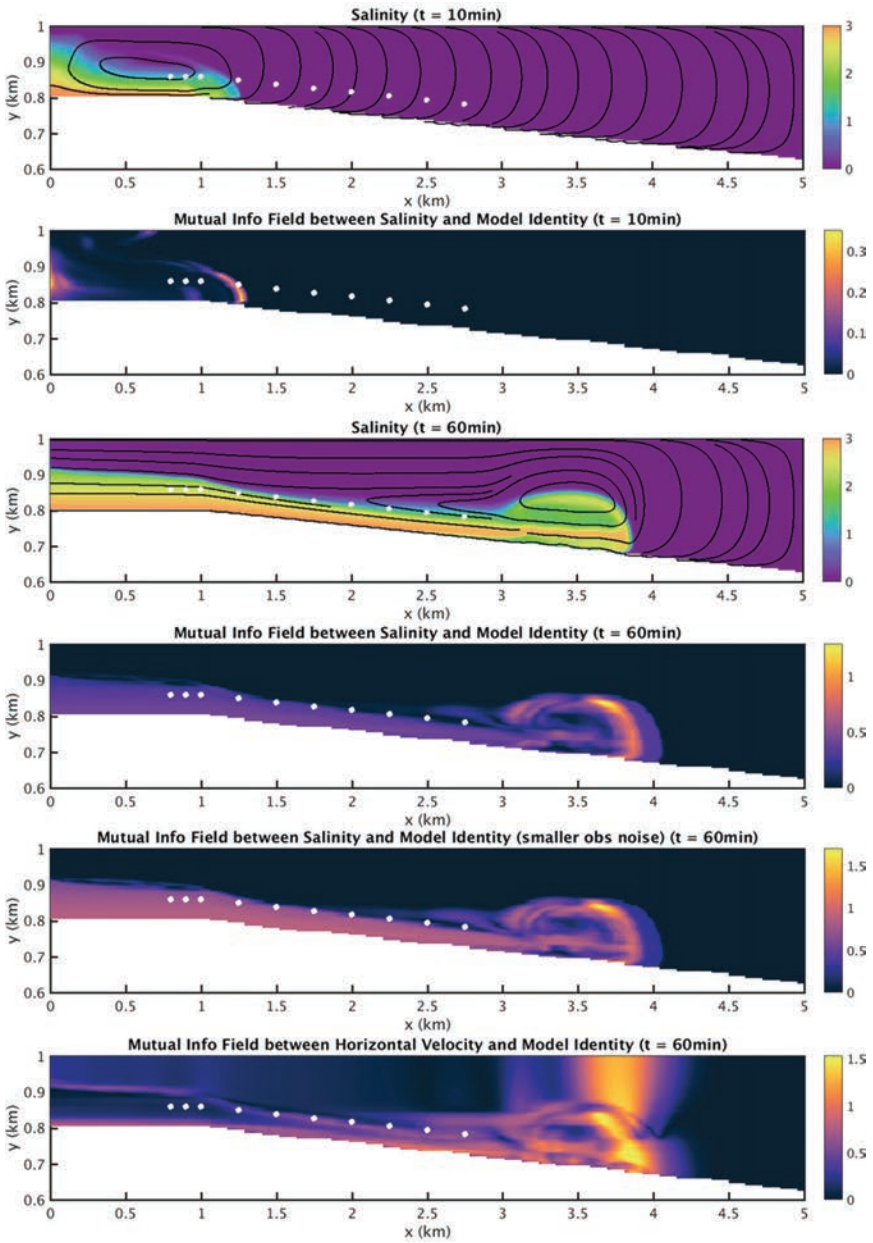

Figure 10. Illustration of how our GMM-DO filter and mutual information predict the most informative data for model learning. A a non-hydrostatic bottom gravity current simulation is used, where salty water flows down the slope from the top left. Different models with different slope angles and different salinity anomaly magnitudes and profiles are proposed. The first and third panels show the salinity field of the simulated ground-truth at $t = 10$ min and $t = 60$ min, respectively, overlaid with streamlines of the velocity field. The second and fourth panels show the mutual information field between salinity and model identity at the same two time instances. The fifth panel is the same as the fourth except that the observation noise variance is smaller. The sixth panel shows the mutual information between the horizontal velocity and the model identity also at $t = 60$ min.

The second and fourth panels of Figure 10 show how an expert system could adjust the observation locations to obtain more informative data for model learning than the heuristic locations indicated by the 10 white dots. Indeed, at both times $t = 10$ min and $t = 60$ min, the high mutual information regions lie in the head of the gravity current and also to a lesser extent near the bottom within the gravity current. At time $t = 10$ min, the inlet is also more informative but less so at $t = 60$ min. All these data locations predicted to be most informative would best reveal the slope angle and the magnitude and profile of the initial salinity anomaly. The fifth panel illustrates the effects of observation noise magnitude on the mutual information field. It is like the fourth panel except for the assumed observation noise standard deviation, which is $\sigma_{\text{noise}} = 0.2$ psu for the fourth panel and $\sigma_{\text{noise}} = 0.1$ psu for the fifth. We can see that with smaller observation noise, the magnitude of mutual information increases. When the observation noise is larger, the signal-to-noise ratio decreases and the information is blurred by the noise. Consistent with this intuition, the mutual information is smaller in this case.

The sixth panel of Figure 10 shows the mutual information field between horizontal velocity and model identity at $t = 60$ min, with the assumed observation noise standard deviation being $\sigma_{\text{noise}} = 0.05$ m/s. The pattern of high-mutual-information region for horizontal velocity is found to be very different from that for salinity. Because a reverse flow above the head of the gravity current is formed due to the conservation of mass, measuring the horizontal velocity above the head should also tell us how fast the current is and thus allow us to infer how salty the water is. The high mutual information region above the head as shown in the sixth panel confirms this physical intuition. Moreover, by comparing the fourth, fifth, and sixth panels, we can also identify which state variable to measure depending on our sensing precision for each of them.

ii. Optimal observations for estimating ecosystem parameters and fields. In the second application, we also utilized the GMM-DO methodology (Sondergaard and Lermusiaux 2013a, b), but now performed data assimilation for the simultaneous estimation of state variables, parameters, and model equations themselves. For the latter, the computing machine learns by discriminating among different but compatible biological models that have the same state variables, but different or not-present ecosystem functions (Gupta 2016). The representative test case in Figure 11 involves a non-dimensional biological model coupled with a dynamical ocean flow in a two-dimensional domain with a seamount/sill, which can create an upwelling of nutrients, leading to phytoplankton bloom. In the top three panels of Figure 11, we show sample non-dimensionalized nutrient, phytoplankton and zooplankton fields, respectively, of a three-component Nutrient-Phytoplankton-Zooplankton model (Franks 2002) simulation. The flow is from left to right, and the phytoplankton bloom in the lee of the seamount, at locations where both light and nutrients are sufficient, is clearly visible. Behind the seamount, the nutrients are reduced while phytoplankton and zooplankton have increased, but with different field structures due to the interplay of the nonlinear biogeochemical and advection terms.

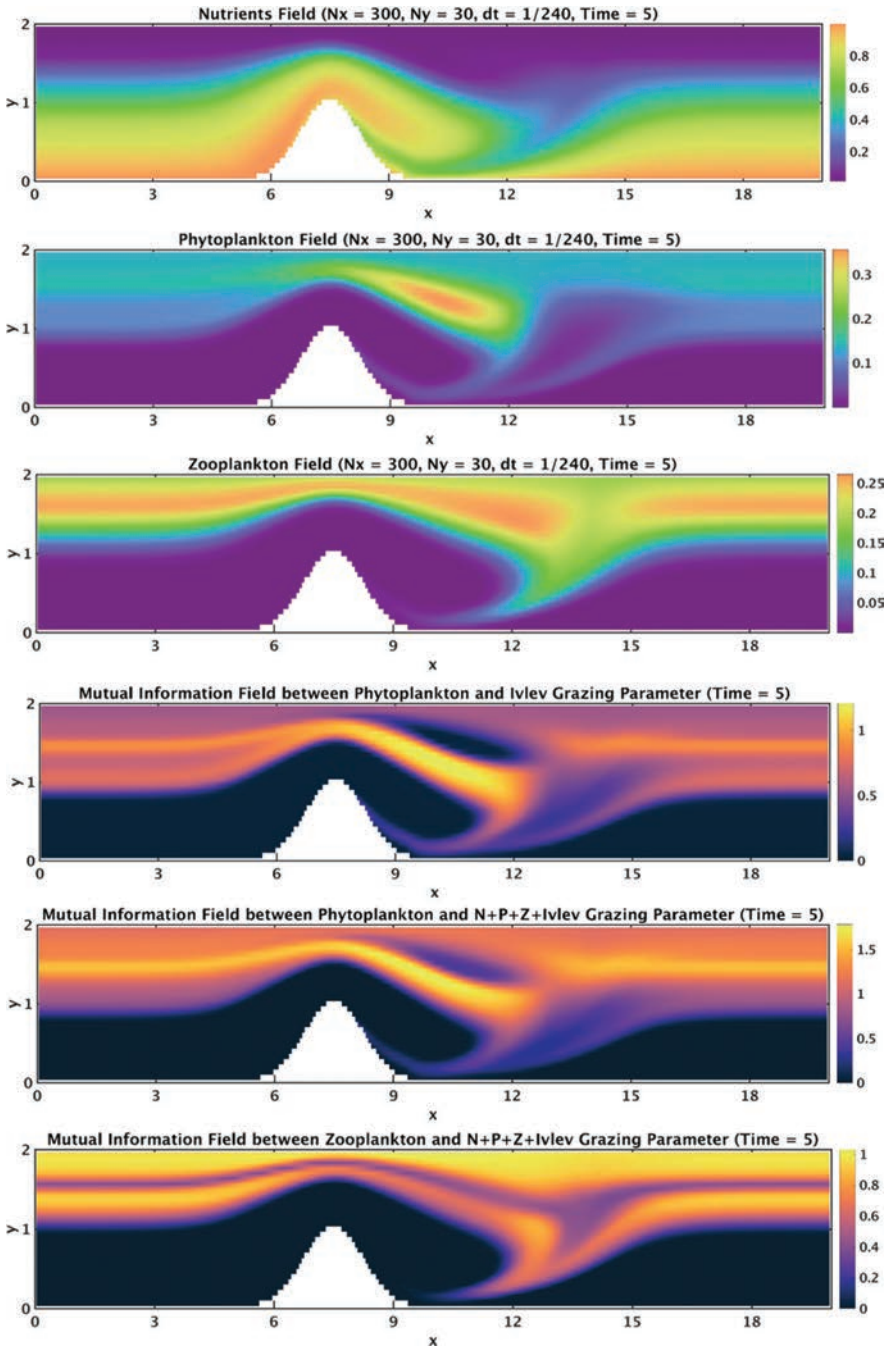

Figure 11. The top three panels shows typical nutrient, phytoplankton and zooplankton fields respectively, for a NPZ model. The fourth panel shows the predicted mutual information field between phytoplankton and the Ivlev grazing parameter, and the fifth/sixth panels show mutual information between phytoplankton/zooplankton, with the three biological NPZ states and the Ivlev grazing parameter combined. These mutual information fields predict the most informative data locations that best estimate just the Ivlev parameter or all the biological states and the Ivlev parameter simultaneously.

To investigate the most informative measurements for such coupled dynamics and simultaneous estimation, we now predict several mutual information fields using equations (10) and (11). An observation noise variance of $\sigma^2_{\text{noise}} = 0.001$ is used for the measured non dimensionalized biology state variables; this amounts to about 30% and 50% of the standard deviation of the variability of phytoplankton and zooplankton, respectively.

First, we consider the scientific goal of measuring phytoplankton at the location that best informs the value of the Ivlev grazing parameter (controlling the rate of phytoplankton grazing by zooplankton). The prior for this parameter is assumed to be uniformly distributed between a fixed range of values. To achieve this goal rigorously, we compute the corresponding mutual information (fourth panel from top in Fig. 11) quantifying the information contained in phytoplankton measurements about the estimation of this Ivlev grazing. As is described in Section 2bii, the mutual information is computed by first fitting a GMM to the samples of random variables involved to obtain the joint probability distribution, and then by numerically integrating the probabilities in equation (10) using a Monte Carlo method. The results (fourth panel) indicate that observations in the bloom region (but not exactly coinciding with the bloom itself) and within a thin strip in the middle of euphotic zone near inflow and outflow are the most sensitive to the Ivlev parameter. Secondary weaker thin strips of high information value are also visible and they correspond to higher spatial gradients of phytoplankton (second panel). It has been verified that assimilating observations located in the higher mutual information region indeed led to the greater decrease in the root-mean-square-error (RMSE) and other skill metrics for the estimated parameter (not shown).

The most informative regions and the amount of information content is dependent on the state(s) being observed, and the scientific or learning goals (Section 2b). To illustrate this property, we compute mutual information fields to predict the phytoplankton or zooplankton (fifth and sixth panel, respectively, in Fig. 11) locations that are overall the most informative for the simultaneous learning of the complete set of biological state variables (N, P, and Z), and of the Ivlev parameter. Results show that in the phytoplankton case (fifth panel), in addition to the bloom region, the area just around the critical depth is also informative for the simultaneous estimation of the states and parameter. Measuring zooplankton (sixth panel) is however overall less informative than phytoplankton for that scientific goal, but the extent of the high mutual information region is much larger, including the whole of upper euphotic zone, but just excluding the area corresponding to maximum zooplankton concentration. We note that predicting such Bayesian fields of mutual information among measured data and a set of variables, regardless of their type and dimension (e.g., more than two), is not feasible with correlations and other commonly used Gaussian quantities.

iii. Optimal observations for estimating coherent structures. In the third application, we utilize the Bayesian GMM-DO data-assimilation and inference engine for the joint estimation of Eulerian variables (e.g., velocity or scalar field at a fixed location) and Lagrangian variables (e.g., drifter/float positions, trajectories, Lagrangian Coherent Structures (LCSs),

etc.). LCSs are defined as the most influential and persistent material surfaces in a flow (Haller 2015; Peacock and Haller 2013). They have been utilized to study varied fluid flow transport and advection of materials in the natural and man-made flows. Most popular methods used to identify LCSs rely on the computation of finite-time Lyapunov exponent (FTLE) or finite-size Lyapunov exponent (FSLE). Next, we illustrate how the GMM-DO and mutual information inference schemes can predict the locations of salinity or velocity observations that would be most informative about velocity or LCS in realistic multiscale ocean fields. The application region is the Northern Arabian Sea of the NASCar field experiment (as in Section 3a), over the time period of 27 to 30 March, 2017.

To predict the ocean probabilities needed for computing mutual information using equations (10) and (11), a 50-member ensemble forecast issued with the ESSE methodology is employed. The ensemble forecast was initialized using a multiscale scheme and historical CTD synoptic data (Lermusiaux, Anderson, and Lozano 2000; Lermusiaux 2002, 2007; Lermusiaux et al. 2017a). In Figure 12, a particular realization of the ensemble is illustrated using the initial (27 March 2017) and forecast (30 March 2017) surface salinity and velocity fields. The white box marks the region for which the zoomed-in fields are shown on the right. A salinity intrusion is visible in this small domain on 30 March 2017. Higher magnitudes of velocity can also be observed along the edge of this salinity intrusion, in accord with geostrophy. The forward-time FTLE field realization shown is over the same interval of three days (27–30 March 2017). The ridges of the forward-time FTLE field correspond with repelling LCSs, which are transport barriers between hyperbolic trajectories. To illustrate the value of such Lagrangian analysis, most of the features of this FTLE field here cannot be easily associated with specific velocity structures. This is because the surface velocity field varied rapidly during 27 to 30 March 2017, due to surface winds, upper-ocean dynamics, and geostrophic turbulence.

In Figure 13, we show forecast mutual information fields between candidate observations of salinity or velocity anywhere in the small domain (marked by the white box in Fig. 12), and the verification variable, which is a field defined over the whole small domain. The observation noise standard deviation for salinity and velocity is set as 30% of the standard deviation in the variability of these fields. These variabilities turn out to have very close numerical values (0.166 PSU for salinity and 0.168 m/s for velocity). For salinity and velocity, the observation noise variance is thus set to $\sigma^2_{\text{noise}} = 0.0025$. The mutual information field between salinity and the scalar field of zonal velocity over the small domain indicates that the most informative salinity data locations are around $(12.6°N, 58.2°E)$. This is on the strongest surface salinity front, i.e., the western edge of the high salinity intrusion (shown in second row of Fig. 12). The mutual information field between salinity and the coherent structures over the small domain predicts the most informative salinity data locations to be are around $(12.5°N, 58.7°E)$, and overall along all of the gradients of surface salinity. We note that the two fields show that most information observation locations for one verification variable may not be so for another. When the observation variable is

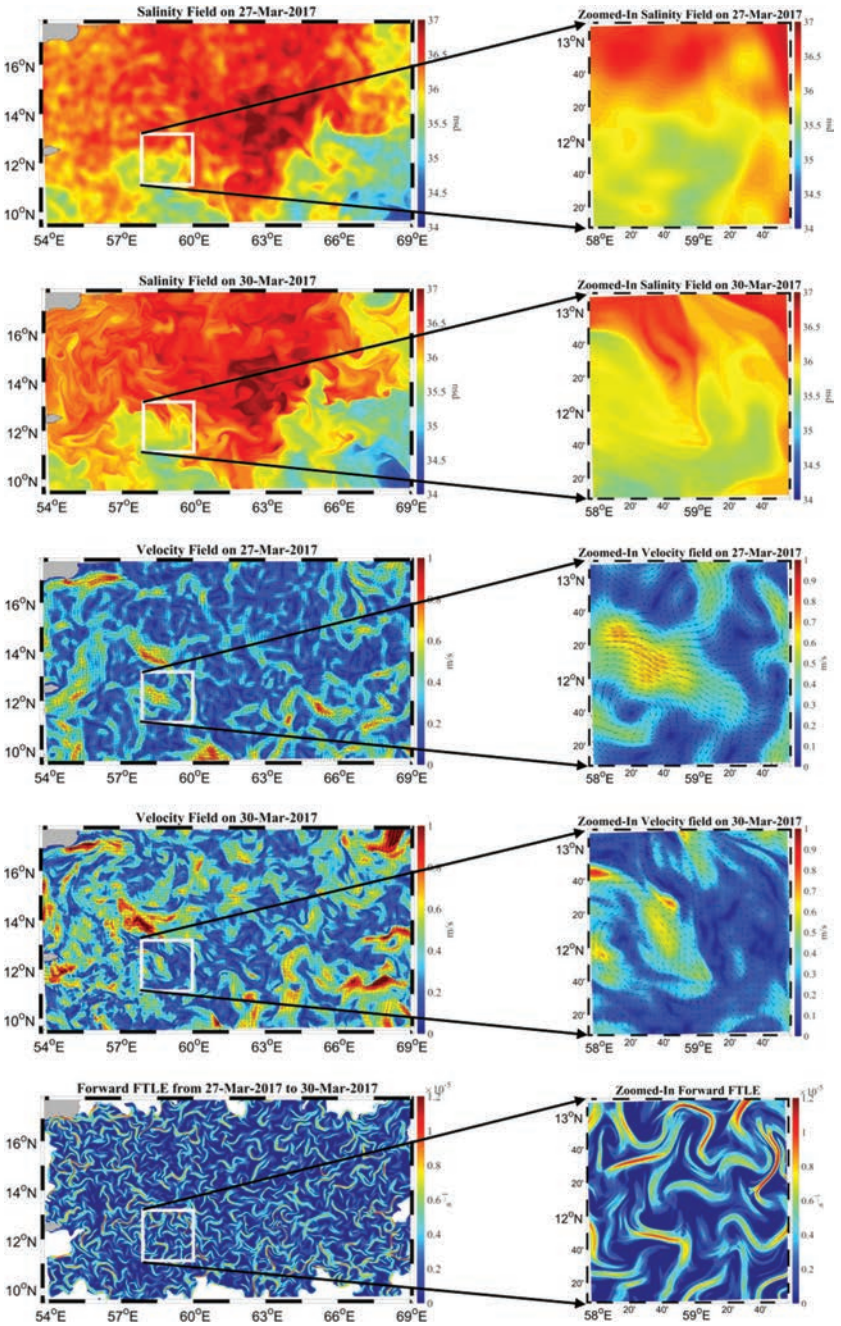

Figure 12. MIT-MSEAS PE forecast realizations of salinity, velocity and forward-time FTLE fields for the main and zoomed NASCar domains. Realizations of the following variables over the period 27–30 March 2017 are shown (top to bottom) with a zoomed-in view to the right (domain marked by the white box on the left): (i) salinity on 27 March 2017, (ii) salinity on 30 March 2017, (iii) velocity on 27 March 2017, (iv) velocity on 30 March 2017, and (v) forward-time FTLE for 27–30 March 2017.

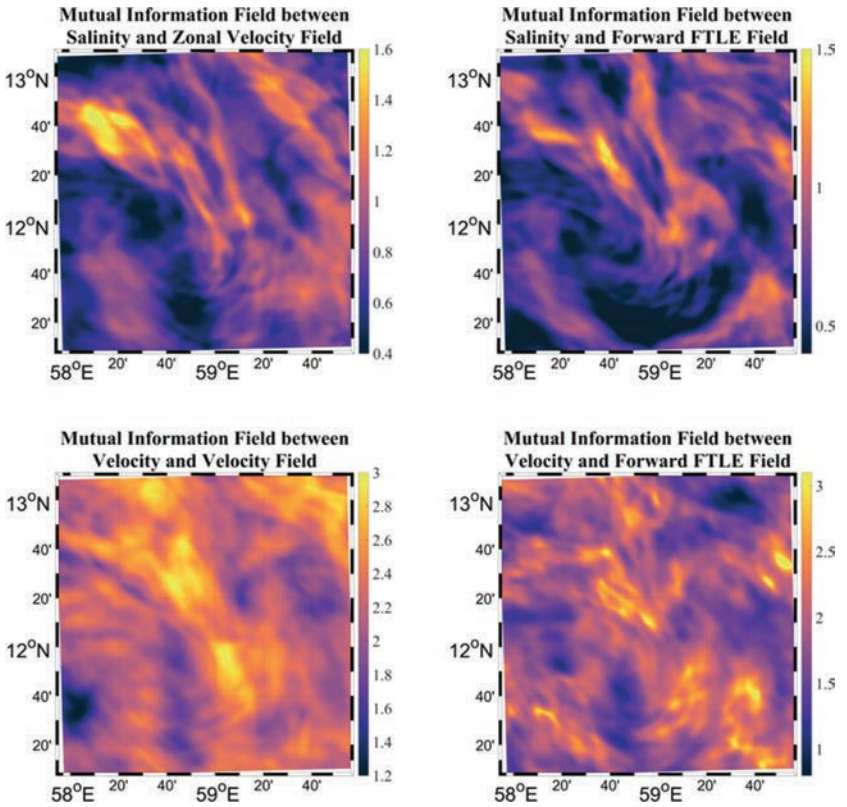

Figure 13. Adaptive sampling predictions for velocity or coherent structure fields for the zoomed NASCar domain. The four mutual information fields are between each of the following pairs of observation and verification variables (from first to second row, and from left to right): (i) salinity and zonal velocity field, (ii) salinity and forward-time FTLE field, (iii) velocity (both components) and velocity field, and (iv) velocity (both components) and forward-time FTLE field. These mutual information fields forecast the most informative observation locations for estimating the verification variable over the small domain (shown in Fig. 12).

velocity and the verification variable is the velocity field (u, v), the mutual information field is more uniform and of larger magnitude than when observing only salinity, as expected. This is also because we measure both u and v, i.e., two variables instead of one. Informative observation locations are around ($12.3°N$,$58.8°E$), ($11.8°N$,$59.2°E$), and ($13°N$,$59.8°E$). Similarly, there are more candidate observation locations that are highly informative about coherent structures when measuring velocity than when measuring salinity. The maxima of the mutual information in this case are around ($12.3°N$, $58.8°E$) and ($11.7°N$, $59.6°E$).

4. Conclusions

Guided by ocean science and applications, critical questions to be answered by intelligent autonomous observing systems are where, when, and what to sample for optimal information, and how to optimally reach the sampling locations. Definitions, concepts, and reproducible progress towards answering these questions using quantitative predictions and fundamental principles were reviewed. Mathematical and practical results in reachability and path planning, adaptive sampling, machine learning, and teaming machines with scientists were overviewed. To provide expert autonomous observing systems, the integrated use of new fundamental differential equations and theories from ocean modeling, data assimilation, control, information science, and machine learning was shown to be essential.

Several recent at-sea campaigns and realistic simulations were utilized to showcase present and future systems. We first demonstrated our exact time-optimal planning theory and tested its applicability for real-time operations in multiple sea exercises in Buzzards Bay and Vineyard Sound. In races between two identical AUVs, it was found that our predicted time-optimal paths (computed by integrating ocean modeling with optimal predictive control) were always faster than the shortest distance paths. The time-optimal path also avoided currents that were strong enough to cause an abort in the AUV following the shortest distance path. The forecasted velocities compared well with the velocities observed by the AUVs, which is encouraging for the future of integrating coastal ocean predictions with rigorous optimal path planning. We then showcased deterministic and probabilistic three-dimensional reachability and path forecasts issued daily for gliders and floats operating for two months in the northern Arabian Sea. These predictions were enabled by high-resolution probabilistic ESSE ensemble ocean forecasts. Based on comparisons to the actual subsequent vehicle tracks, the probabilistic reachability planning system showed predictive skill for long periods of time. It was useful to the vehicle operators. Finally, novel Bayesian adaptive sampling for hypothesis testing and optimal learning was illustrated. Computing machines were shown to forecast the observations that were most informative to estimate the accuracy of model formulations, the values of ecosystem parameters and dynamics fields, and the presence of Lagrangian coherent structures in the flow.

It is worth noting that if ocean fields were oversampled and everything was measured in time and space, there would be little need for smart sampling. In all other cases, because not all data are equally informative about specific scientific objectives, intelligent observing systems are critical. For example, when ship surveys consisted of vertical sampling along rectilinear sections, this was because researchers wanted such estimates (based on their scientific objectives or ship constraints) or because not all of what researchers knew was utilized to design and adapt the surveys in an optimal, expert way. Indeed, in conducting sampling campaigns, all prior knowledge (fundamental conservation laws, model equations, uncertainty estimates, past observations, control laws, etc.) should be employed. Using this knowledge as prior inputs, the most informative sampling plans should then be predicted

by optimizing objective criteria rooted in fundamental information theory, Bayesian data assimilation, uncertainty quantification, and machine learning. Even in pure exploration of the unknown, as soon as one observation is collected and analyzed, knowledge is acquired and plans should at least be reviewed in the above rigorous ways.

In the past, rigorous equations and efficient methods for reachability, path planning, and adaptive sampling did not exist. Due to limited computational and robotics capabilities, some scientists and operators made approximate choices in guiding robotic observing systems. Examples of such approximations include the following: ignoring the highly variable ocean dynamics or the ocean flow transports, linearizing model equations, assuming steady or Gaussian statistics, using ineffective or inaccurate planning algorithms, or reducing control theory equations to heuristics and simplified schemes. Interdisciplinary teams and multidisciplinary education were not common. Often these approximations and issues limited the efficacy of the path planning and adaptive sampling. However, we showed in the present examples that the most informative observation can commonly be 50% to 150% more informative than an average observation. When observations are sparse and expensive, such improvements motivate the need for intelligent sampling.

The new quantitative methods and fundamental equations reviewed and showcased in the present work provide a modern basis for the inference engine and knowledge base of expert predicting and observing systems. The dynamically orthogonal (DO) differential equations of the ocean modeling system provide an optimally-reduced and nonlinear prediction of the prior probability distribution of the ocean state, parameters, and other secondary variables. The Gaussian mixture model (GMM)-DO filter and smoother then capture the non-Gaussian statistics when it occurs and assimilate the data by Bayesian updates of the prior probability distribution. The GMM-DO schemes allow the efficient computation of the mutual information among any vectors of candidate observation variables and the scientific quantities of interest. The resulting dynamic mutual information fields are then used to objectively and autonomously predict the optimal future sampling plans. This optimization is completed in accord with the capabilities of the ocean sampling vehicles by using a modified Hamilton–Jacobi level-set equation that governs their reachable set and reachability front. Variations of this equation and the corresponding backward tracking equation can forecast the time-optimal, energy-optimal, or risk-optimal ocean paths, in 2-d or 3-d in space and for varied vehicles and robotic motions. When combined with the mutual information criteria for optimal sampling, the integrated system predicts where, when, and what to sample.

Our outlook is that reproducible scientific models, efficient control equations, increasing computational power, novel communication capabilities, thriving machine learning, and decision-making ability of humans will continue to be integrated to form intelligent autonomous ocean predicting and observing systems. Such interdisciplinary research adventures should be gripping. The results will benefit marine exploration and exploitation for both science and engineering, including societal applications in energy, food, security, and ultimately the sustainability of our oceans and environment.

Acknowledgments. We are thankful to all members of the MSEAS group, past and present. We thank Prof. A. Gangopadhyay for useful discussions on the Indian ocean. We are grateful to Drs. J. Edwards, J. Smith, N. Pulsone, and the captain and crew of the R/V Discovery. We thank the HYCOM team for their real-time ocean fields; M. Pyle and E. Rogers of NCEP for their real-time HIRESW and GFSp25 atmospheric flux forecasts, and the Fleet Numerical Meteorology and Oceanography Center (FNMOC) for their real-time NAVGEM 0.5-degree atmospheric flux forecasts through usgodae.org. We are grateful to the Office of Naval Research for support under grants N00014-14-1-0476 (Science of Autonomy - LEARNS), N00014-15-1-2616 (NASCar-OPS), and N00014-14-1-0725 (Bays-DA) to the Massachusetts Institute of Technology (MIT). We especially thank Drs. T. Paluszkiewicz, M. Steinberg, and S. Harper, for their support and interactions. We thank the National Oceanographic Partnership Program (NOPP) for research support under grant N00014-15-1-2597 (Seamless Multiscale Forecasting), the Naval Research Laboratory for research support under grant N00173-13-2-C009, and the Technology and Contracts Office at MIT Lincoln Laboratory. We also thank the MIT-Tata Center Program for the Fellowship support of DNS. PFJL thanks his parents and family for their support even in difficult times.

REFERENCES

Abbott, M. R., K. H. Brink, C. R. Booth, D. Blasco, L. A. Codispoti, P. P. Niiler, and S. R. Ramp. 1990. Observations of phytoplankton and nutrients from a Lagrangian drifter off northern California. J. Geophys. Res.: Oceans, *95*(C6), 9393–9409. doi: 10.1029/JC095iC06p09393

Aghababa, M. P. 2012. Finite-time chaos control and synchronization of fractional-order nonautonomous chaotic (hyperchaotic) systems using fractional nonsingular terminal sliding mode technique. Nonlinear Dyn., *69*(1), 247–261. doi: 10.1007/s11071-011-0261-6

Alvarez, A., A. Caiti, and R. Onken. 2004. Evolutionary path planning for autonomous underwater vehicles in a variable ocean. IEEE J. Ocean. Eng., *29*(2), 418–429. doi: 10.1109/JOE.2004.827837

Babanin, A. V., A. van der Westhuysen, D. Chalikov, and W. E. Rogers. 2017. Advanced wave modeling, including wave-current interaction, *in* The Sea: The Science of Ocean Prediction, part 1. Special issue, J. Mar. Res., *75*, 239–262.

Bachmayer, R., N. E. Leonard, J. Graver, E. Fiorelli, P. Bhatta, and D. Paley. 2004. Underwater gliders: Recent developments and future applications, *in* Proc. IEEE International Symposium on Underwater Technology, 195–200.

Bahr, A., J. J. Leonard, and M. F. Fallon. 2009. Cooperative localization for autonomous underwater vehicles. Int. J. Rob. Res., *28*(6), 714–728. doi: 10.1177/0278364908100561

Baker, N. L. and R. Daley. 2000. Observation and background adjoint sensitivity in the adaptive observation-targeting problem. Q. J. R. Meteorol. Soc., *126*(565), 1431–1454. doi: 10.1002/qj.49712656511

Bakolas, E. and P. Tsiotras. 2010. The Zermelo–Voronoi diagram: A dynamic partition problem. Automatica, *46*(12), 2059–2067. doi: 10.1016/j.automatica.2010.09.003

Bellingham, J. G. and K. Rajan. 2007. Robotics in remote and hostile environments. Science, *318* (5853), 1098–1102. doi: 10.1126/science.1146230

Bellingham, J. G., C. Goudey, T. Consi, and C. Chryssostomidis. 1992. A small, long-range autonomous vehicle for deep ocean exploration, *in* The Second International Offshore and Polar Engineering Conference. International Society of Offshore and Polar Engineers.

Benjamin, M. R., H. Schmidt, P. M. Newman, and J. J. Leonard. 2010. Nested autonomy for unmanned marine vehicles with MOOS-IvP. J. Field Robot., *27*(6), 834–875. doi: 10.1002/rob.20370

Bergot, T., G. Hello, A. Joly, and S. Malardel. 1999. Adaptive observations: A feasibility study. Mon. Weather Rev., *127*(5), 743–765. doi: 10.1175/1520-0493(1999)127<0743:AOAFS>2.0.CO;2

Bertino, L. and M. M. Holland. 2017. Coupled ice-ocean modeling and predictions, *in* The Sea: The Science of Ocean Prediction, part 2. Special issue, J. Mar. Res., *75*.

Bishop, C. H., B. J. Etherton, and S. J. Majumdar. 2001. Adaptive sampling with the ensemble transform Kalman filter. Part I: Theoretical aspects. Mon. Weather Rev., *129*(3), 420–436. doi: 10.1175/1520-0493(2001)129<0420:ASWTET>2.0.CO;2

Boyd, T., M. Inall, E. Dumont, and C. Griffiths. 2010. AUV observations of mixing in the tidal outflow from a scottish sea loch, *in* Proc. 2010 IEEE/OES Autonomous Underwater Vehicles, 1–9.

Brizzolara, S. and R. A. Brizzolara. 2016. Autonomous sea surface vehicles, *in* Springer Handbook of Ocean Engineering. New York: Springer, 323–340.

Bryson, A. E. 1975. *Applied optimal control: Optimization, estimation and control*. Boca Raton: CRC Press.

Buizza, R. and A. Montani. 1999. Targeting observations using singular vectors. J. Atmos. Sci., *56* (17), 2965–2985. doi: 10.1175/1520-0469(1999)056<2965:TOUSV>2.0.CO;2

Carragher, P., G. Hine, P. Legh-Smith, J. Mayville, R. Nelson, S. Pai, I. Parnum et al. 2013. A new platform for offshore exploration and production. Oilfield Rev., *2014*(25), 4.

Carrassi, A., A. Trevisan, and F. Uboldi. 2007. Adaptive observations and assimilation in the unstable subspace by breeding on the data-assimilation system. Tellus A, *59*(1), 101–113. doi: 10.1111/j.1600-0870.2006.00210.x

Carroll, K. P., S. R. McClaran, E. L. Nelson, D. M. Barnett, D. K. Friesen, and G. William. 1992. AUV path planning: An A* approach to path planning with consideration of variable vehicle speeds and multiple, overlapping, time-dependent exclusion zones, *in* Proc. 1992 IEEE Symposium on Autonomous Underwater Vehicle Technology, 79–84.

Centurioni, L., A. Horányi, C. Cardinali, E. Charpentier, and R. Lumpkin. 2017a. A global ocean observing system for measuring sea level atmospheric pressure: Effects and impacts on numerical weather prediction. Bull. Am. Meteorol. Soc., *98*(2), 231–238. doi: 10.1175/BAMS-D-15-00080.1

Centurioni, L., V. Hormann, L. Talley, and I. Arzeno, L. Beal, M. Caruso, P. Conry et al. 2017b. Northern Arabian Sea Circulation Autonomous Research (NASCar): A research initiative based on autonomous sensors. Oceanography, *30*(2), 74–87. doi: 10.5670/oceanog.2017.224

Choi, H.-L. and J. P. How. 2010. Continuous trajectory planning of mobile sensors for informative forecasting. Automatica, *46*(8), 1266–1275. doi: 10.1016/j.automatica.2010.05.004

Cover, T. M. and J. A. Thomas. 1991. Elements of Information Theory, 1st ed. New York: John Wiley and Sons.

Crandall, M. G. and P.-L. Lions. 1983. Viscosity solutions of Hamilton-Jacobi equations. Trans. Amer. Math. Soc., *277*(1), 1–42. doi: 10.1090/S0002-9947-1983-0690039-8

Crimmins, D. M., C. T. Patty, M. A. Beliard, J. Baker, J. C. Jalbert, R. J. Komerska, S. G. Chappell, and D. R. Blidberg. 2006. Long-endurance test results of the solar-powered AUV system, *in* Proc. OCEANS 2006 MTS/IEEE, 1–5. doi: 10.1109/OCEANS.2006.306997

Cummings, J. A. and O. M. Smedstad. 2013. Variational data assimilation for the global ocean, *in* Data Assimilation for Atmospheric, Oceanic and Hydrologic Applications, vol 2. New York: Springer, 303–343.

Curcio, J., J. Leonard, J. Vaganay, A. Patrikalakis, A. Bahr, D. Battle, H. Schmidt, and M. Grund. 2005. Experiments in moving baseline navigation using autonomous surface craft, *in* Proc. OCEANS 2005 MTS/IEEE, 730–735. doi: 10.1109/OCEANS.2005.1639839

Curtin, T. B. and J. G. Bellingham. 2009. Progress toward autonomous ocean sampling networks. Deep Sea Res. Part II Top. Stud. Oceanogr., *56*(3), 62–67. doi: 10.1016/j.dsr2.2008.09.005

Curtin, T. B., J. G. Bellingham, J. Catipovic, and D. Webb. 1993. Autonomous oceanographic sampling networks. Oceanography, *6*(3), 86–94. doi: 10.5670/oceanog.1993.03

Daescu, D. N. and I. M. Navon. 2004. Adaptive observations in the context of 4D-Var data assimilation. Meteorol. Atmos. Phys., *85*(4), 205–226. doi: 10.1007/s00703-003-0011-5

Daniel, T., J. Manley, and N. Trenaman. 2011. The Wave Glider: Enabling a new approach to persistent ocean observation and research. Ocean Dyn., *61*(10), 1509–1520. doi: 10.1007/s10236-011-0408-5

Das, J., F. Py, J. B. Harvey, J. P. Ryan, A. Gellene, R. Graham, D. A. Caron et al. 2015. Data-driven robotic sampling for marine ecosystem monitoring. Int. J. Robot. Res., *34*(12), 1435–1452. doi: 10.1177/0278364915587723

Davis, R. E. 1991. Lagrangian ocean studies. Ann. Rev. Fluid Mech., *23*(1), 43–64.

Davis, R. E., N. E. Leonard, and D. M. Fratantoni. 2009. Routing strategies for underwater gliders. Deep Sea Res. Part II Top. Stud. Oceanogr., *56*(3), 173–187. doi: 10.1016/j.dsr2.2008.08.005

Davis, R. E., M. D. Ohman, D. L. Rudnick, and J. T. Sherman. 2008. Glider surveillance of physics and biology in the southern California Current System. Limnol. Oceanogr., *53*(5part2), 2151–2168. doi: 10.4319/lo.2008.53.5_part_2.2151

Davis, R., J. Sherman, and J. Dufour. 2001. Profiling ALACEs and other advances in autonomous subsurface floats. J. Atmos. Ocean. Technol., *18*(6), 982–993. doi: 10.1175/1520-0426(2001)018<0982:PAAOAI>2.0.CO;2

Dhanak, M. R. and N. I. Xiros. 2016. Springer Handbook of Ocean Engineering. New York: Springer.

Dickey, T. D. 2003. Emerging ocean observations for interdisciplinary data assimilation systems. J. Mar. Syst., *40*, 5–48. doi: 10.1016/S0924-7963(03)00011-3

Dickey, T., E. Itsweire, M. Moline, and M. Perry. 2008. Introduction to the Limnology and Oceanography Special Issue on Autonomous and Lagrangian Platforms and Sensors (ALPS). Limnol. Oceanogr., *53*(5part2), 2057–2061. doi: 10.4319/lo.2008.53.5_part_2.2057

Edwards, J., J. Smith, A. Girard, D. Wickman, D. N. Subramani, C. S. Kulkarni, J. P. J. Haley et al. 2017. Data-driven learning and modeling of AUV operational characteristics for optimal path planning, *in* OCEANS '17 MTS/IEEE Conference.

Egbert, G. D. and S. Y. Erofeeva. 2002. Efficient inverse modeling of barotropic ocean tides. J. Atmos. Ocean. Technol., *19*(2), 183–204. doi: 10.1175/1520-0426(2002)019<0183:EIMOBO>2.0.CO;2

Egbert, G. D. and S. Y. Erofeeva. 2013. OSU tidal inversion. http://volkov.oce.orst.edu/tides/tpxo8_atlas.html

Egbert, G. D. and R. D. Ray. 2017. Tidal prediction, *in* The Sea: The Science of Ocean Prediction, part 1. Special issue, J. Mar. Res., *75*, 189–237.

Ehrendorfer, M. and J. J. Tribbia. 1997. Optimal prediction of forecast error covariances through singular vectors. J. Atmos. Sci., *54*(2), 286–313.

Elisseeff, P., H. Schmidt, M. Johnson, D. Herold, N. Chapman, and M. McDonald. 1999. Acoustic tomography of a coastal front in Haro Strait, British Columbia. J. Acoustic. Soc. Am., *106*(1), 169–184. doi: 10.1121/1.427046

Environmental Modeling Center, 2003. The GFS Atmospheric Model. NCEP Office Note 442, Global Climate and Weather Modeling Branch, EMC, Camp Springs, Maryland. http://www.emc.ncep.noaa.gov/officenotes/newernotes/on442.pdf

Eriksen, C. C., T. J. Osse, R. D. Light, T. Wen, T. W. Lehman, P. L. Sabin, J. W. Ballard, and A. M. Chiodi. 2001. Seaglider: A long-range autonomous underwater vehicle for oceanographic research. IEEE J. Ocean. Eng., *26*(4), 424–436. doi: 10.1109/48.972073

Farrar, J. T., L. Rainville, A. J. Plueddemann, W. S. Kessler, C. Lee, B. A. Hodges, R. W. Schmitt, J. B. Edson, S. C. Riser et al. 2015. Salinity and temperature balances at the SPURS central mooring during fall and winter. Oceanography, *28*(1), 56–65. doi: 10.5670/oceanog.2015.06

Feppon, F. and P. F. J. Lermusiaux. 2018a. A geometric approach to dynamical model-order reduction. J. Matrix Anal. Appl., In press.

Feppon, F. and P. F. J. Lermusiaux. 2018b. Dynamically orthogonal numerical schemes for efficient stochastic advection and Lagrangian transport. SIAM Rev. Soc. Ind. Appl. Math., In press.

Ferrari, S., G. Foderaro, P. Zhu, and T. A. Wettergren. 2016. Distributed optimal control of multiscale dynamical systems: A tutorial. IEEE Control Syst., *36*(2), 102–116. doi: 10.1109/MCS.2015.2512034

Fiorelli, E., N. E. Leonard, P. Bhatta, D. A. Paley, R. Bachmayer, and D. M. Fratantoni. 2006. Multi-AUV control and adaptive sampling in Monterey Bay. IEEE J. Ocean. Eng., *31*(4), 935–948. doi: 10.1109/JOE.2006.880429

Franks, P. J. 2002. NPZ models of plankton dynamics: Their construction, coupling to physics, and application. J. Oceanogr., *58*(2), 379–387. doi: 10.1023/A:1015874028196

Freitag, L., M. Grund, C. Von Alt, R. Stokey, and T. Austin. 2005. A shallow water acoustic network for mine countermeasures operations with autonomous underwater vehicles. Underwater Defense Technology (UDT), 1–6.

Frolov, S., B. Garau, and J. Bellingham. 2014. Can we do better than the grid survey: Optimal synoptic surveys in presence of variable uncertainty and decorrelation scales. J. Geophys. Res.: Oceans, *119* (8), 5071–5090. doi: 10.1002/2013JC009521

Garau, B., M. Bonet, A. Alvarez, S. Ruiz, and A. Pascual. 2009. Path planning for autonomous underwater vehicles in realistic oceanic current fields: Application to gliders in the western Mediterranean Sea. J. Marit. Res., *6*(2), 5–22.

Gawarkiewicz, G., S. Jan, P. F. J. Lermusiaux, J. L. McClean, L. Centurioni, K. Taylor, B. Cornuelle et al. 2011. Circulation and intrusions northeast of Taiwan: Chasing and predicting uncertainty in the cold dome. Oceanography, *24*(4), 110–121. doi: 10.5670/oceanog.2011.99

Glenn, S. M., T. D. Dickey, B. Parker, and W. Boicourt. 2000. Long-term real-time coastal ocean observation networks. Oceanography, *13*(1), 24–34. doi: 10.5670/oceanog.2000.50

Graham, R. and J. Cortés. 2012. Cooperative adaptive sampling of random fields with partially known covariance. Int. J. Robust Nonlin., *22*(5), 504–534. doi: 10.1002/rnc.1710

Griffiths, G., R. Davis, C. Eriksen, D. Frye, P. Marchand, T. Dickey, and R. Weller. 2001. Towards new platform technology for sustained observations, *in* Observing the Ocean for Climate in the 21st Century, C. J. Koblinsky and N. R. Smith, eds. Melbourne: GODAE, Bureau of Meteorology, 324–338.

Gupta, A., 2016. Bayesian inference of obstacle systems and coupled biogeochemical-physical models. Master's thesis, Indian Institute of Technology, Kanpur, India.

Haidvogel, D. B., E. N. Cuchitser, S. Danilov, and B. Fox-Kemper. 2017. Numerical Modelling in a Multi-Scale Ocean. In *The Sea: The Science of Ocean Prediction,* part 2. Special issue, *Journal of Marine Research 75*.

Haley, Jr., P. J., A. Agarwal, and P. F. J. Lermusiaux. 2015. Optimizing velocities and transports for complex coastal regions and archipelagos. Ocean Model., *89*, 1–28. doi: 10.1016/j.ocemod.2015.02.005

Haley, Jr., P. J. and P. F. J. Lermusiaux. 2010. Multiscale two-way embedding schemes for free-surface primitive equations in the "Multidisciplinary Simulation, Estimation and Assimilation System". Ocean Dyn., *60*(6), 1497–1537. doi: 10.1007/s10236-010-0349-4

Haley, Jr., P. J., P. F. J. Lermusiaux, A. R. Robinson, W. G. Leslie, O. Logoutov, G. Cossarini, X. S. Liang et al. 2009. Forecasting and reanalysis in the Monterey Bay/California Current region for the Autonomous Ocean Sampling Network-II experiment. Deep Sea Res. Part II Top. Stud. Oceanogr., *56*(3–5), 127–148. doi: 10.1016/j.dsr2.2008.08.010

Haller, G. 2015. Lagrangian coherent structures. Ann. Rev. Fluid Mech., *47*, 137–162. doi: 10.1146/annurev-fluid-010313-141322

Heaney, K. D., G. Gawarkiewicz, T. F. Duda, and P. F. J. Lermusiaux. 2007. Nonlinear optimization of autonomous undersea vehicle sampling strategies for oceanographic data-assimilation. J. Field Robot., *24*(6), 437–448. doi: 10.1002/rob.20183

Heaney, K. D., P. F. J. Lermusiaux, T. F. Duda, and P. J. Haley, Jr. 2016. Validation of genetic algorithm based optimal sampling for ocean data assimilation. Ocean Dyn., *66*, 1209–1229. doi: 10.1007/s10236-016-0976-5

Heidemann, J., M. Stojanovic, and M. Zorzi. 2011. Underwater sensor networks: Applications, advances and challenges. Philos. Trans. R. Soc Lond. A, *370*(1958), 158–175. doi: 10.1098/rsta.2011.0214

Hogan, T. F., M. Liu, J. A. Ridout, M. S. Peng, T. R. Whitcomb, B. C. Ruston, C. A. Reynolds et al. 2014. The Navy Global Environmental Model. Oceanography, *27*(3), 116–125. doi: 10.5670/oceanog.2014.73

Hollinger, G. A., A. A. Pereira, J. Binney, T. Somers, and G. S. Sukhatme. 2016. Learning uncertainty in ocean current predictions for safe and reliable navigation of underwater vehicles. J. Field Robot., *33*(1), 47–66. doi: 10.1002/rob.21613

Hsieh, M. A., E. Forgoston, T. W. Mather, and I. B. Schwartz. 2012. Robotic manifold tracking of coherent structures in flows. *In* 2012 IEEE International Conference on Robotics and Automation, pages 4242–4247. doi: 10.1109/ICRA.2012.6224769

Inanc, T., S. C. Shadden, and J. E. Marsden. 2005. Optimal trajectory generation in ocean flows, *in* Proc. 2005 American Control Conference, 674–679. doi: 10.1109/ACC.2005.1470035

Jackson, P. 1998. Introduction to Expert Systems, 3rd ed. Boston: Addison-Wesley Longman.

Jacobs, G. and B. Fox-Kemper. 2017. Ocean dynamics, *in* The Sea: The Science of Ocean Prediction, part 2. Special issue, J. Mar. Res., *75*.

Jaffe, J. S., P. J. Franks, P. L. Roberts, D. Mirza, C. Schurgers, R. Kastner, and A. Boch. 2017. A swarm of autonomous miniature underwater robot drifters for exploring submesoscale ocean dynamics. Nat. Commun., *8*, 14189. doi: 10.1038/ncomms14189

Jiménez, S., T. De La Rosa, S. Fernández, F. Fernández, and D. Borrajo. 2012. A review of machine learning for automated planning. Knowl. Eng. Rev., *27*(4), 433–467. doi: 10.1017/S0269888912000001X

Johnston, T. and D. Rudnick. 2015. Mixing estimates in the California Current System from sustained observations by underwater gliders. Deep Sea Res. Part II Top. Stud. Oceanogr., *112*, 61–78. doi: 10.1016/j.dsr2.2014.03.009

Jones, D. and G. A. Hollinger. 2017. Planning energy-efficient trajectories in strong disturbances. IEEE Robot. Autom. Lett., *2*(4), 2080–2087. doi: 10.1109/LRA.2017.2719760

Kalnay, E. 2003. Atmospheric Modeling, Data Assimilation, and Predictability. New York: Cambridge university press.

Kruger, D., R. Stolkin, A. Blum, and J. Briganti. 2007. Optimal AUV path planning for extended missions in complex, fast-flowing estuarine environments, *in* Proc. 2007 IEEE International Conference on Robotics and Automation, pages 4265–4270. doi: 10.1109/ROBOT.2007.364135

Kulkarni, C. S., 2017. Three-dimensional time-optimal path planning in dynamic and realistic environments. Master's thesis, Massachusetts Institute of Technology, Department of Mechanical Engineering, Cambridge, MA.

Kulkarni, C. and P. F. J. Lermusiaux. 2018. Three-dimensional time-optimal path planning in the realistic ocean. In preparation.

Latombe, J.-C. 1991. *Robot Motion Planning*. Norwell, MA: Kluwer Academic Publishers.

LaValle, S. M. 2006. *Planning Algorithms*. New York: Cambridge University Press.

Lavender, K. L., R. E. Davis, and W. B. Owens. 2002. Observations of open-ocean deep convection in the Labrador Sea from subsurface floats. J. Phys. Oceanogr., *32*(2), 511–526. doi: 10.1175/1520-0485(2002)032<0511:OOOODC>2.0.CO;2

Leonard, J. J. and A. Bahr. 2016. Autonomous underwater vehicle navigation, *in* Springer Handbook of Ocean Engineering. New York: Springer, 341–358.

Leonard, N. E., D. A. Paley, R. E. Davis, D. M. Fratantoni, F. Lekien, and F. Zhang. 2010. Coordinated control of an underwater glider fleet in an adaptive ocean sampling field experiment in Monterey Bay. J. Field Robot., *27*(6), 718–740. doi: 10.1002/rob.20366

Leonard, N. E., D. A. Paley, F. Lekien, R. Sepulchre, D. M. Fratantoni, and R. E. Davis. 2007. Collective motion, sensor networks, and ocean sampling. Proc. IEEE, *95*(1), 48–74. doi: 10.1109/JPROC.2006.887295

Lermusiaux, P. F. J. 1999a. Estimation and study of mesoscale variability in the Strait of Sicily. Dynam. Atmos. Ocean., *29*(2), 255–303. doi: 10.1016/S0377-0265(99)00008-1

Lermusiaux, P. F. J. 1999b. Data assimilation via Error Subspace Statistical Estimation, part II: Mid-Atlantic Bight shelfbreak front simulations, and ESSE validation. Mon. Weather Rev., *127*(7), 1408–1432. doi: 10.1175/1520-0493(1999)127<1408:DAVESS>2.0.CO;2

Lermusiaux, P. F. J. 2002. On the mapping of multivariate geophysical fields: Sensitivities to size, scales, and dynamics. J. Atmos. Ocean. Technol., *19*(10), 1602–1637. doi: 10.1175/1520-0426(2002)019<1602:OTMOMG>2.0.CO;2

Lermusiaux, P. F. J. 2006. Uncertainty estimation and prediction for interdisciplinary ocean dynamics. J. Comput. Phys., *217*(1), 176–199. doi: 10.1016/j.jcp.2006.02.010

Lermusiaux, P. F. J. 2007. Adaptive modeling, adaptive data assimilation and adaptive sampling. Physica D, *230*(1), 172–196. doi: 10.1016/j.physd.2007.02.014

Lermusiaux, P. F. J., D. G. M. Anderson, and C. J. Lozano. 2000. On the mapping of multivariate geophysical fields: Error and variability subspace estimates. Q. J. R. Meteorol. Soc., *126*(565), 1387–1429. doi: 10.1002/qj.49712656510

Lermusiaux, P. F. J., C.-S. Chiu, G. G. Gawarkiewicz, P. Abbot, A. R. Robinson, R. N. Miller, P. J. Haley, Jr. et al. 2006. Quantifying uncertainties in ocean predictions. Oceanography, *19*(1), 92–105. doi: 10.5670/oceanog.2006.93

Lermusiaux, P. F. J., P. J. Haley, Jr., S. Jana, A. Gupta, C. S. Kulkarni, C. Mirabito, W. H. Ali et al. 2017a. Optimal planning and sampling predictions for autonomous and lagrangian platforms and sensors in the northern Arabian Sea. Oceanography, *30*(2), 172–185. doi: 10.5670/oceanog.2017.242

Lermusiaux, P. F. J., P. J. Haley Jr., S. Jana, A. Gupta, C. Kulkarni, D. Subramani, C. Mirabito, and W. H. Ali. 2017b. NASCar-OPS sea exercise 17, arabian sea february-march 2017. http://mseas.mit.edu/Sea_exercises/NASCar-OPS-17/

Lermusiaux, P. F. J., T. Lolla, P. J. Haley, Jr., K. Yigit, M. P. Ueckermann, T. Sondergaard, and W. G. Leslie. 2016. Science of autonomy: Time-optimal path planning and adaptive sampling for swarms of ocean vehicles, *in* Springer Handbook of Ocean Engineering: Autonomous Ocean Vehicles, Subsystems and Control, T. Curtin, ed. New York: Springer, 481–498.

Lermusiaux, P. F. J. and A. R. Robinson. 1999. Data assimilation via Error Subspace Statistical Estimation, part I: Theory and schemes. Mon. Weather Rev., *127*(7), 1385–1407. doi: 10.1175/1520-0493(1999)127<1385:DAVESS>2.0.CO;2

Leslie, W. G., P. J. Haley, Jr., P. F. J. Lermusiaux, M. P. Ueckermann, O. Logutov, and J. Xu. 2010. MSEAS Manual. MSEAS Report 06, Department of Mechanical Engineering, Massachusetts Institute of Technology, Cambridge, MA. http://mseas.mit.edu/?p=2237

Liu, Z., Y. Zhang, X. Yu, and C. Yuan. 2016. Unmanned surface vehicles: An overview of developments and challenges. Annu. Rev. Control, *41*, 71–93. doi: 10.1016/j.arcontrol.2016.04.018

Logutov, O. G. and P. F. J. Lermusiaux. 2008. Inverse barotropic tidal estimation for regional ocean applications. Ocean Model., *25*(1–2), 17–34. doi: 10.1016/j.ocemod.2008.06.004

Lolla, T. 2016. Path Planning and Adaptive Sampling in the Coastal Ocean. Ph.D. thesis, Massachusetts Institute of Technology, Department of Mechanical Engineering, Cambridge, MA.

Lolla, T., P. F. J. Lermusiaux, M. P. Ueckermann, and P. J. Haley, Jr. 2014a. Time-optimal path planning in dynamic flows using level set equations: Theory and schemes. Ocean Dyn., *64*(10), 1373–1397. doi: 10.1007/s10236-014-0757-y

Lolla, T., P. J. Haley, Jr., and P. F. J. Lermusiaux. 2014b. Time-optimal path planning in dynamic flows using level set equations: Realistic applications. Ocean Dyn., *64*(10), 1399–1417. doi: 10.1007/s10236-014-0760-3

Lolla, T. and P. F. J. Lermusiaux. 2017a. A Gaussian mixture model smoother for continuous nonlinear stochastic dynamical systems: Theory and scheme. Mon. Weather Rev., *145*, 2743–2761. doi: 10.1175/MWR-D-16-0064.1

Lolla, T. and P. F. J. Lermusiaux. 2017b. A Gaussian mixture model smoother for continuous nonlinear stochastic dynamical systems: Applications. Mon. Weather Rev., *145*, 2763–2790. doi: 10.1175/MWR-D-16-0065.1

Lolla, T., M. P. Ueckermann, K. Yiğit, P. J. Haley, Jr., and P. F. J. Lermusiaux. 2012. Path planning in time dependent flow fields using level set methods, *in* 2012 IEEE International Conference on Robotics and Automation, pages 166–173. doi: 10.1109/ICRA.2012.6225364

Lolla, T. and P. F. J. Lermusiaux. 2018. A forward reachability equation for minimum-time path planning in strong dynamic flows. SIAM J. Control Optim. Sub-judice. In preparation.

Lolla, T., P. J. Haley, Jr., and P. F. J. Lermusiaux. 2015. Path planning in multiscale ocean flows: coordination and dynamic obstacles. Ocean Modelling, *94*, 46–66. doi: 10.1016/j.ocemod.2015.07.013

Lorenz, E. N. and K. A. Emanuel. 1998. Optimal sites for supplementary weather observations: Simulation with a small model. J. Atmos. Sci., *55*(3), 399–414. doi: 10.1175/1520-0469(1998)055<0399:OSFSWO>2.0.CO;2

Lucas, A. J., J. D. Nash, R. Pinkel, J. A. MacKinnon, A. Tandon, A. Mahadevan, M. M. Omand et al. 2016. Adrift upon a salinity-stratified sea: A view of upper-ocean processes in the Bay of Bengal during the southwest monsoon. Oceanography, *29*(2), 134–145. doi: 10.5670/oceanog.2016.46

Lumpkin, R. and M. Pazos. 2007. Measuring surface currents with surface velocity program drifters: the instrument, its data, and some recent results, *in* Lagrangian Analysis and Prediction of Coastal and Ocean Dynamics, A. Griffa, A. D. Kirwan, A. Mariano, T. Özgökmen, and T. Rossby, eds. New York: Cambridge University Press, 39–67.

Mahadevan, A., E. D'Asaro, C. Lee, and M. J. Perry. 2012. Eddy-driven stratification initiates North Atlantic spring phytoplankton blooms. Science, *337*(6090), 54–58. doi: 10.1126/science.1218740

Mahmoudian, N. and C. Woolsey. 2008. Underwater glider motion control, *in* 2008 IEEE Conference on Decision and Control, 552–557. doi: 10.1109/CDC.2008.4739432

Manley, J. E. 2004. Multiple AUV missions in the national oceanic and atmospheric administration, *in* 2004 IEEE Xplore Conference: Autonomous Underwater Vehicles, 20–25. doi: 10.1109/AUV.2004.1431188

Manley, J. and S. Willcox. 2010. The wave glider: A persistent platform for ocean science, *in* OCEANS 2010 IEEE Sydney, 1–5. doi: 10.1109/OCEANSSYD.2010.5603614

Mannarini, G., G. Coppini, R. Lecci, and G. Turrisi. 2017. Sea currents and waves for optimal route planning with VISIR, *in* 16th International Conference on Computer and IT Applications in the Maritime Industries, 170–179.

Mannarini, G., G. Turrisi, A. D'Anca, M. Scalas, N. Pinardi, G. Coppini, F. Palermo et al. 2016. VISIR: Technological infrastructure of an operational service for safe and efficient navigation in the Mediterranean Sea. Nat. Hazard. Earth Sys., *16*(8), 1791–1806. doi: 10.5194/nhess-16-1791-2016

Martin, J. P., C. M. Lee, C. C. Eriksen, C. Ladd, and N. B. Kachel. 2009. Glider observations of kinematics in a Gulf of Alaska eddy. J. Geophys. Res.: Oceans, *114*(C12), C12021. doi: 10.1029/2008JC005231

McGann, C., F. Py, K. Rajan, and A. G. Olaya. 2009. Integrated planning and execution for robotic exploration, *in* HYCAS 2009 1st International Workshop on Hybrid Control of Autonomous Systems Integrating Learning, Deliberation and Reactive Control, 33.

Meyer, D. 2016. Glider technology for ocean observations: A review. Ocean Sci. Discuss., *2016*, 1–26. doi: 10.5194/os-2016-40

Michini, M., M. A. Hsieh, E. Forgoston, and I. B. Schwartz. 2014. Robotic tracking of coherent structures in flows. IEEE Trans. Robot., *30*(3), 593–603. doi: 10.1109/TRO.2013.2295655

Miller, A. J., M. Collins, S. Gualdi, T. G. Jensen, V. Misra, L. P. Pezzi, D. W. Pierce et al. 2017. Coupled ocean-atmosphere modeling and predictions, *in* The Sea: The Science of Ocean Prediction, part 1. Special issue, J. Mar. Res., *75*, 361–402.

Mirabito, C., D. N. Subramani, T. Lolla, P. J. Haley, Jr., A. Jain, P. F. J. Lermusiaux, C. Li et al. June 2017. Autonomy for surface ship interception, *in* OCEANS '17 MTS/IEEE Aberdeen. doi: 10.1109/OCEANSE.2017.8084817

Munafò, A., E. Simetti, A. Turetta, A. Caiti, and G. Casalino. 2011. Autonomous underwater vehicle teams for adaptive ocean sampling: a data-driven approach. Ocean Dyn., *61*(11), 1981–1994. doi: 10.1007/s10236-011-0464-x

National Centers for Environmental Prediction (NCEP). 2017. High-resolution window (HIRESW) forecast system. http://www.nco.ncep.noaa.gov/pmb/products/hiresw/

Nicholson, J. and A. Healey. 2008. The present state of autonomous underwater vehicle (AUV) applications and technologies. Mar. Technol. Soc. J., *42*(1), 44–51. doi: 10.4031/002533208786861272

Niiler, P. 2001. Chapter 4.1 The world ocean surface circulation. International Geophysics, *77*, 193–204. doi: 10.1016/S0074-6142(01)80119-4

Özgökmen, T. M. and E. P. Chassignet. 2002. Dynamics of two-dimensional turbulent bottom gravity currents. J. Phys. Oceanogr., *32*(5), 1460–1478. doi: 10.1175/1520-0485(2002)032<1460:DOTDTB>2.0.CO;2

Paley, D. A., F. Zhang, and N. E. Leonard. 2008. Cooperative control for ocean sampling: The glider coordinated control system. IEEE Trans. Control Syst. Technol., *16*(4), 735–744. doi: 10.1109/TCST.2007.912238

Palmer, T. N., R. Gelaro, J. Barkmeijer, and R. Buizza. 1998. Singular vectors, metrics, and adaptive observations. J. Atmos. Sci., *55*(4), 633–653. doi: 10.1175/1520-0469(1998)055<0633:SVMAAO>2.0.CO;2

Peacock, T. and G. Haller. 2013. Lagrangian coherent structures: The hidden skeleton of fluid flows. Phys. Today, *66*(2), 41. doi: 10.1063/PT.3.1886

Penland, C. and A. Navarra. 2017. Issues in stochastic ocean modeling, *in* The Sea: The Science of Ocean Prediction, part 2. Special issue, J. Mar. Res., *75*.

Pentland, A. 2014. Social Physics: How Good Ideas Spread the Lessons from a New Science. London: Penguin.

Petres, C., Y. Pailhas, P. Patron, Y. Petillot, J. Evans, and D. Lane. 2007. Path planning for autonomous underwater vehicles. IEEE Trans. Robot., *23*(2), 331–341. doi: 10.1109/TRO.2007.895057

Pinkel, R., M. A. Goldin, J. A. Smith, O. M. Sun, A. A. Aja, M. N. Bui, and T. Hughen. 2011. The Wirewalker: A vertically profiling instrument carrier powered by ocean waves. J. Atmos. Ocean. Technol., *28*(3), 426–435. doi: 10.1175/2010JTECHO805.1

Pullen, J., R. Allard, H. Seo, A. J. Miller, S. Chen, L. P. Pezzi, T. Smith et al. 2017. Coupled ocean-atmosphere forecasting at short and medium time scales, *in* The Sea: The Science of Ocean Prediction, part 2. Special issue, J. Mar. Res., *75*.

Rainville, L., C. M. Lee, D. L. Rudnick, and K.-C. Yang. 2013. Propagation of internal tides generated near luzon strait: Observations from autonomous gliders. J. Geophys. Res., *118*(9), 4125–4138. doi: 10.1002/jgrc.20293

Ramp, S. R., R. E. Davis, N. E. Leonard, I. Shulman, Y. Chao, A. R. Robinson et al. 2009. Preparing to predict: The second Autonomous Ocean Sampling Network (AOSN-II) experiment in the Monterey Bay. Deep Sea Res. Part II Top. Stud. Oceanogr., *56*(3–5), 68–86. doi: 10.1016/j.dsr2.2008.08.013

Rao, D. and S. B. Williams. 2009. Large-scale path planning for underwater gliders in ocean currents, *in* Australasian Conference on Robotics and Automation (ACRA).

Riser, S. C., H. J. Freeland, D. Roemmich, S. Wijffels, A. Troisi, M. Belbéoch, D. Gilbert et al. 2016. Fifteen years of ocean observations with the global Argo array. Nat. Clim. Chang., *6*(2), 145–153. doi: 10.1038/nclimate2872

Robinson, A. and S. Glenn. 1999. Adaptive sampling for ocean forecasting. Nav. Res. Rev., *51*(2), 26–38. doi: 10.1007/978-3-642-35088-7_16

Robinson, A. R. and P. F. J. Lermusiaux. 2002. Data assimilation for modeling and predicting coupled physical–biological interactions in the sea, *in* Biological–Physical Interactions in the Sea. The Sea, vol 12. A. R. Robinson, J. J. McCarthy, and B. J. Rothschild, eds. New York: John Wiley and Sons, 475–536.

Robinson, A. R., P. F. J. Lermusiaux, and N. Q. Sloan, III. 1998. Data assimilation, *in* The Global Coastal Ocean. Processes and Methods. The Sea, vol 10. K. H. Brink and A. R. Robinson, eds. New York: John Wiley and Sons, 541–594.

Roemmich, D., O. Boebel, Y. Desaubies, H. Freeland, K. Kim, B. King, P.-Y. Le Traon et al. 2001. Argo: The global array of profiling floats, *in* Observing the Ocean for Climate in the 21st Century. C. Koblinsky and N. Smith, eds. Melbourne: GODAE, Bureau of Meteorology.

Roemmich, D., G. C. Johnson, S. Riser, R. Davis, J. Gilson, W. B. Owens, S. L. Garzoli et al. 2009. The Argo program: Observing the global ocean with profiling floats. Oceanography, *22*(2), 34–43. doi: 10.5670/oceanog.2009.36

Roemmich, D., S. Riser, R. Davis, and Y. Desaubies. 2004. Autonomous profiling floats: Workhorse for broad-scale ocean observations. Mar. Technol. Soc. J., *38*(2), 21–29.

Roy, N., H.-L. Choi, D. Gombos, J. Hansen, J. How, and S. Park. 2007. Adaptive observation strategies for forecast error minimization, *in* Proc. 7th International Conference on Computational Science. Y. Shi, G. D. van Albada, J. Dongarra, and P. M. A. Sloot, eds. Berlin, Heidelberg: Springer, 1138–1146. doi: 10.1007/978-3-540-72584-8_149

Rudnick, D. L. 2016. Ocean research enabled by underwater gliders. Ann. Rev. Mar. Sci., *8*(1), 519–541. doi: 10.1146/annurev-marine-122414-033913

Rudnick, D. L., R. E. Davis, C. C. Eriksen, D. M. Fratantoni, and M. J. Perry. 2004. Undersea gliders for ocean research. Mar. Technol. Soc. J., *38*(2), 73–84.

Rudnick, D. and M. Perry. 2003. ALPS: Autonomous and lagrangian platforms and sensors, *in* Workshop Report, vol 64. Boulder: University Corporation for Atmospheric Research.

Russell, S. and P. Norvig. 2009. *Artificial Intelligence: A Modern Approach*, 3rd ed. Upper Saddle River, NJ: Prentice Hall Press.

Sapsis, T. P. and P. F. J. Lermusiaux. 2009. Dynamically orthogonal field equations for continuous stochastic dynamical systems. Physica D, *238*(23–24), 2347–2360. doi: 10.1016/j.physd.2009.09.017

Särkkä, S. 2013. Bayesian Filtering and Smoothing. Number 3. New York: Cambridge University Press.

Schmidt, H., J. G. Bellingham, M. Johnson, D. Herold, D. M. Farmer, and R. Pawlowicz. 1996. Real-time frontal mapping with AUVs in a coastal environment, *in* Proc. OCEANS 96 MTS/IEEE Conference. The Coastal Ocean: Prospects for the 21st Century, volume 3, pages 1094–1098. doi: 10.1109/OCEANS.1996.569054

Schmidt, H., M. R. Benjamin, S. M. Petillo, and R. Lum. 2016. Nested autonomy for distributed ocean sensing, *in* Springer Handbook of Ocean Engineering, M. R. Dhanak and N. I. Xiros, eds. New York: Springer, 459–480.

Schofield, O., S. Glenn, J. Orcutt, M. Arrott, M. Meisinger, A. Gangopadhyay, W. Brown et al. 2010. Automated sensor network to advance ocean science. Eos, *91*(39), 345–346. doi: 10.1029/2010EO390001

Schofield, O., J. Kohut, D. Aragon, L. Creed, J. Graver, C. Haldeman, J. Kerfoot et al. 2007. Slocum gliders: Robust and ready. J. Field Robot., *24*(6), 473–485. doi: 10.1002/rob.20200

Schott, F. A. and J. P. McCreary. 2001. The monsoon circulation of the indian ocean. Prog. Oceanogr., *51*(1), 1–123. doi: 10.1016/S0079-6611(01)00083-0

Sethian, J. A. 1999. Fast marching methods. SIAM Rev., *41*(2), 199–235. doi: 10.1137/S0036144598347059

Shcherbina, A. Y., M. A. Sundermeyer, E. Kunze, E. D'Asaro, G. Badin, D. Birch, A.-M. E. G. Brunner-Suzuki et al. 2015. The LatMix summer campaign: Submesoscale stirring in the upper ocean. Bull. Am. Meteorol. Soc., *96*(8), 1257–1279. doi: 10.1175/BAMS-D-14-00015.1

Sherman, J., R. E. Davis, W. B. Owens, and J. Valdes. 2001. The autonomous underwater glider "Spray". IEEE J. Ocean. Eng., *26*(4), 437–446. doi: 10.1109/48.972076

Smith, W. H. and D. T. Sandwell. 1997. Global sea floor topography from satellite altimetry and ship depth soundings. Science, *277*(5334), 1956–1962.

Smith, R. N., M. Schwager, S. L. Smith, B. H. Jones, D. Rus, and G. S. Sukhatme. 2011. Persistent ocean monitoring with underwater gliders: Adapting sampling resolution. J. Field Robot., *28*(5), 714–741. doi: 10.1002/rob.20405

Sondergaard, T. and P. F. J. Lermusiaux. 2013a. Data assimilation with Gaussian mixture models using the dynamically orthogonal field equations. Part I: Theory and scheme. Mon. Weather Rev., *141*(6), 1737–1760. doi: 10.1175/MWR-D-11-00295.1

Sondergaard, T. and P. F. J. Lermusiaux. 2013b. Data assimilation with Gaussian mixture models using the dynamically orthogonal field equations. Part II: Applications. Mon. Weather Rev., *141*(6), 1761–1785. doi: 10.1175/MWR-D-11-00296.1

Sonnenburg, C. R. and C. A. Woolsey. 2013. Modeling, identification, and control of an unmanned surface vehicle. J. Field Robot., *30*(3), 371–398. doi: 10.1002/rob.21452

Soulignac, M., P. Taillibert, and M. Rueher. 2009. Time-minimal path planning in dynamic current fields, *in* 2009 IEEE International Conference on Robotics and Automation, 2473–2479. doi: 10.1109/ROBOT.2009.5152426

Steinberg, M. 2006. Intelligent autonomy for unmanned naval vehicles, *in* Proc. SPIE 6230, Unmanned Systems Technology VIII. doi: 10.1117/12.665870

St Laurent, L. C. and A. M. Thurnherr. 2007. Intense mixing of lower thermocline water on the crest of the Mid-Atlantic Ridge. Nature, *448*(7154), 680. doi: 10.1038/nature06043

Stommel, H. 1989. The slocum mission. Oceanography, *2*(1), 22–25.

Subramani, D. N., P. J. Haley, Jr., and P. F. J. Lermusiaux. 2017. Energy-optimal path planning in the coastal ocean. J. Geophys. Res.: Oceans, *122*, 3981–4003. doi: 10.1002/2016JC012231

Subramani, D. N. and P. F. J. Lermusiaux. 2016. Energy-optimal path planning by stochastic dynamically orthogonal level-set optimization. Ocean Model., *100*, 57–77. doi: 10.1016/j.ocemod.2016.01.006

Subramani, D. N., P. F. J. Lermusiaux, P. J. Haley, Jr., C. Mirabito, S. Jana, C. S. Kulkarni, A. Girard et al. 2017. Time-optimal path planning: Real-time sea exercises, *in* OCEANS '17 MTS/IEEE Aberdeen. doi: 10.1109/OCEANSE.2017.8084776

Subramani, D. N., Q. J. Wei, and P. F. J. Lermusiaux. 2018. Stochastic time-optimal path-planning in uncertain, strong, and dynamic flows. Comput. Methods Appl. Mech. Eng. In press.

Sun, W., P. Tsiotras, T. Lolla, D. N. Subramani, and P. F. J. Lermusiaux. 2017a. Pursuit-evasion games in dynamic flow fields via reachability set analysis, *in* 2017 American Control Conference (ACC), 4595–4600. doi: 10.23919/ACC.2017.7963664

Sun, W., P. Tsiotras, T. Lolla, D. N. Subramani, and P. F. J. Lermusiaux. 2017b. Multiple-pursuer-one-evader pursuit evasion game in dynamic flow fields. J. Guid. Control Dyn., *40*(7), 1627–1637 doi: 10.2514/1.G002125

Swallow, J. 1955. A neutral-buoyancy float for measuring deep currents. Deep Sea Res. (1953), *3*(1), 74–81. doi: 10.1016/0146-6313(55)90037-X

Swallow, J., B. McCartney, and N. Millard. 1974. The minimode float tracking system. Deep-Sea Res. Oceanogr. Abstr., *21*(7), 573–595. doi: 10.1016/0011-7471(74)90013-8

Thompson, D., S. Chien, Y. Chao, P. Li, M. Arrott, M. Meisinger, A. Balasuriya et al. 2009. Glider mission planning in a dynamic ocean sensorweb, *in* International Conference on Automated Planning and Scheduling (ICAPS) Workshop on Scheduling and Planning Applications (SPARK).

Thompson, D. R., S. Chien, Y. Chao, P. Li, B. Cahill, J. Levin, O. Schofield, A. Balasuriya et al. 2010. Spatiotemporal path planning in strong, dynamic, uncertain currents, *in* 2010 IEEE International Conference on Robotics and Automation, pages 4778–4783. doi: 10.1109/ROBOT.2010.5509249

Todd, R. E., D. L. Rudnick, M. R. Mazloff, B. D. Cornuelle, and R. E. Davis. 2012. Thermohaline structure in the California Current System: Observations and modeling of spice variance. J. Geophys. Res.: Oceans, *117*(C2), C02008. doi: 10.1029/2011JC007589

Toth, Z. and E. Kalnay. 1997. Ensemble forecasting at NCEP and the breeding method. Mon. Weather Rev., *125*(12), 3297–3319. doi: 10.1175/1520-0493(1997)125<3297:EFANAT>2.0.CO;2

Treguier, A. M., E. P. Chassignet, A. L. Boyer, and N. Pinardi. 2017. Modeling and forecasting the âŁœweather of the oceanâŁž at the mesoscale, *in* The Sea: The Science of Ocean Prediction, part 1. Special issue, *Journal of Marine Research 75*, 301–329.

Ueckermann, M. P. and P. F. J. Lermusiaux. 2012. 2.29 Finite Volume MATLAB Framework Documentation. MSEAS Report 14, Department of Mechanical Engineering, Massachusetts Institute of Technology, Cambridge, MA. http://mseas.mit.edu/?p=2567

Ueckermann, M. P., P. F. J. Lermusiaux, and T. P. Sapsis. 2013. Numerical schemes for dynamically orthogonal equations of stochastic fluid and ocean flows. J. Comput. Phys., *233*, 272–294. doi: 10.1016/j.jcp.2012.08.041

Vasudevan, C. and K. Ganesan. 1994. Case-based path planning for autonomous underwater vehicles, *in* Proc. 1994 IEEE International Symposium on Intelligent Control, 160–165. doi: 10.1109/ISIC.1994.367824

Venkatesan, R., A. Tandon, E. D'Asaro, and M. Atmanand. 2018. *Observing the Oceans in Real Time*, 1st ed. Cham: Springer International Publishing, In press.

Wang, T., O. P. Le Maître, I. Hoteit, and O. M. Knio. 2016. Path planning in uncertain flow fields using ensemble method. Ocean Dyn., *66*(10), 1231–1251. doi: 10.1007/s10236-016-0979-2

Wang, D., P. F. J. Lermusiaux, P. J. Haley, Jr., D. Eickstedt, W. G. Leslie, and H. Schmidt. 2009. Acoustically focused adaptive sampling and on-board routing for marine rapid environmental assessment. J. Mar. Syst., *78*(Supplement), S393–S407. doi: 10.1016/j.jmarsys.2009.01.037

Webb, D. C., P. J. Simonetti, and C. P. Jones. 2001. SLOCUM: An underwater glider propelled by environmental energy. IEEE J. Ocean. Eng., *26*(4), 447–452. doi: 10.1109/48.972077

Wei, Q. J., 2015. Time-optimal path planning in uncertain flow fields using stochastic dynamically orthogonal level set equations. Bachelor's thesis, Massachusetts Institute of Technology, Department of Mechanical Engineering, Cambridge, MA.

Willcox, J. S., J. G. Bellingham, Y. Zhang, and A. B. Baggeroer. 2001. Performance metrics for oceanographic surveys with autonomous underwater vehicles. IEEE J. Ocean. Eng., *26*(4), 711–725. doi: 10.1109/48.972114

Witt, J. and M. Dunbabin. 2008. Go with the flow: Optimal AUV path planning in coastal environments, *in* Proc. 2008 Australasian Conference on Robotics and Automation, Australasian Robotics and Automation Association (ARAA), 1–9.

Wolek, A. and C. A. Woolsey. 2017. Model-based path planning, *in* Sensing and Control for Autonomous Vehicles: Applications to Land, Water and Air Vehicles. T. I. Fossen, K. Y. Pettersen, and H. Nijmeijer, eds. Cham: Springer International Publishing, 183–206. doi: 10.1007/978-3-319-55372-6_9

Xu, J., P. F. J. Lermusiaux, P. J. Haley, Jr., W. G. Leslie, and O. G. Logutov. 2008. Spatial and temporal variations in acoustic propagation during the PLUSNet-07 Exercise in Dabob Bay. Proc. Mtgs. Acoust. *4*(1), 070001. doi: 10.1121/1.2988093

Yan, W., X. Bai, X. Peng, L. Zuo, and J. Dai. 2014. The routing problem of autonomous underwater vehicles in ocean currents, *in* OCEANS 2014 TAIPEI, 1–6. doi: 10.1109/OCEANS-TAIPEI.2014.6964486

Yilmaz, N. K., C. Evangelinos, P. F. J. Lermusiaux, and N. M. Patrikalakis. 2008. Path planning of autonomous underwater vehicles for adaptive sampling using mixed integer linear programming. IEEE J. Ocean. Eng., *33*(4), 522–537. doi: 10.1109/JOE.2008.2002105

Yoo, B. and J. Kim. 2016. Path optimization for marine vehicles in ocean currents using reinforcement learning. J. Mar. Sci. Technol., *21*(2), 334–343. doi: 10.1007/s00773-015-0355-9

Yuh, J. 2000. Design and control of autonomous underwater robots: A survey. Auton. Robots, *8*(1), 7–24. doi: 10.1023/A:1008984701078

Zhang, W., T. Inanc, S. Ober-Blobaum, and J. E. Marsden. 2008. Optimal trajectory generation for a glider in time-varying 2D ocean flows B-spline model, *in* 2008 IEEE International Conference on Robotics and Automation, 1083–1088. doi: 10.1109/ROBOT.2008.4543348

Received: *12 August 2017*; revised: *10 January 2018*.

Editor's note: Contributions to *The Sea: The Science of Ocean Prediction* are being published separately in special issues of *Journal of Marine Research* and will be made available in a forthcoming supplement as Volume 17 of the series.